vehicles

Article

Handling Stability Control for Multi-Axle Distributed Drive Vehicles Based on Model Predictive Control

Hongjie Cheng, Zhenwei Hou *, Zhihao Liu, Jianhua Li, Jiashuo Zhang, Yuan Zhao and Xiuyu Liu

The National Key Discipline Laboratory of Armament Launch Theory & Technology, PLA Rocket Force University of Engineering, Xi'an 710025, China; chenghj_epgc@163.com (H.C.); liuzh_epgc@163.com (Z.L.); lee_jianhua614@163.com (J.L.); zhangjs_epgc@163.com (J.Z.); zy44630@163.com (Y.Z.); liuxiuyu1994@163.com (X.L.)

* Correspondence: hzw_epgc@163.com

Abstract

Multi-axle vehicles are commonly used for heavy-duty special operations, which easily leads to high driving torque demands when adopting distributed electric drive configurations. This study achieves the objective of reducing the driving torque of each in-wheel motor while controlling the stability of multi-axle vehicles. Taking a five-axle distributed drive test vehicle as the research object, a hierarchical control strategy integrating active all-wheel steering and direct yaw moment control is proposed. The upper layer is implemented based on model predictive control, with fuzzy control introduced to dynamically adjust control weights; the lower layer accomplishes the allocation of targets calculated by the upper layer through minimizing the objective function of tire load ratio. A linear parameter varying (LPV) tire model is introduced into the vehicle model to improve the calculation accuracy of tire lateral forces, and a neural network method is employed to solve the real-time performance issue of the model predictive control (MPC) controller. The proposed strategy is verified through a combination of simulation and real vehicle tests. High-speed condition simulations demonstrate that the AWS/DYC strategy significantly outperforms the ARS/DYC approach: compared to the active rear-wheel steering strategy, while the sideslip angle is reduced by 90.98%, the peak driving torque is reduced by 30.78%. Notably, tire slip angle analysis reveals that AWS/DYC maintains relatively uniform slip angle distribution across axles with a maximum of 4.7°, entirely within the linear working region, optimally balancing tire performance utilization with lateral stability while preserving safety margin, whereas ARS/DYC causes slip angles to exceed 11.9° at the rear axle, entering saturation. Low-speed real vehicle tests further confirm the engineering applicability of the strategy. The proposed method is of significant importance for the application of distributed drive configurations in the field of special vehicles.

Keywords: distributed drive vehicle; multi-axle vehicle; active all-wheel steering; direct yaw moment control; neural network; yaw stability

Academic Editors: Richard Romano and Julian F Dunne

Received: 14 November 2025
Revised: 20 January 2026
Accepted: 26 January 2026
Published: 1 February 2026

1. Introduction

Multi-axle heavy-duty vehicles have been a research hotspot due to their poor handling stability caused by factors such as a long body, high center of gravity, and heavy mass [1–3]. The distributed drive chassis structure, with its high controllable degrees of freedom, fast response speed, compact body structure, and high chassis drive-by-wire integration, represents the optimal platform for implementing advanced vehicle dynamics control technologies [4,5]. Each wheel's motor can provide both driving and braking forces, effectively expanding the adaptive range of chassis control systems [6].

Existing research has made certain progress in the field of stability control for distributed electric drive vehicles. Control methods mainly include sliding mode control [7], adaptive control [8], linear optimal control [9], robust control [10], and model predictive control [11,12], along with control architectures primarily based on decentralized [13], centralized [14], and hierarchical [15,16] frameworks. Hierarchical control architecture features mutual independence and functional decoupling between levels, separately considering stability control requirements and torque allocation during design. It also exhibits good robustness to local system failures and certain fault tolerance capabilities, while combining the advantages of both decentralized and centralized architectures with clear structure, facilitating system development and functional expansion [17]. Li et al. [18] proposed a composite electronic torque power steering hierarchical control strategy for multi-axle distributed drive vehicles based on dynamic modeling and analysis, enhancing steering system flexibility and fault tolerance at low speeds while ensuring vehicle stability at high speeds, reducing energy consumption to a certain extent. Shi et al. [19] adopted time-varying model predictive control to track desired states based on the model characteristics of distributed drive three-axle commercial vehicles, achieving steady-state drift path tracking under extreme conditions, expanding the vehicle's controllable stability boundary and reducing the peak torque of in-wheel motors. According to existing research, it is evident that in multi-axle distributed electric drive vehicles, reducing the peak torque of in-wheel motors not only improves vehicle stability margin but also has significant importance for optimizing overall vehicle power consumption. Through reasonable torque distribution strategies, controlling each wheel motor's torque within the efficient operating range can effectively reduce overall system energy consumption and heat dissipation burden. However, the aforementioned studies have not considered the nonlinear factors of multi-axle distributed drive vehicles under actual operating conditions.

With deeper research, handling and stability control technologies considering nonlinear factors and the coordination of various control variables have been successively proposed. Reference [20] proposed an integrated controller including multiple stability control objectives such as longitudinal, lateral, and roll based on the LPV-MPC structure to improve the comprehensive stability performance of four-wheel in-wheel drive electric vehicles, obtaining a linearized tire model through first-order Taylor expansion [21] of the nonlinear tire model. This controller achieves good multi-objective comprehensive control effects under conventional conditions, improving handling stability while suppressing tire slip ratio. Li et al. [22–24] proposed a fast path-tracking strategy based on nonlinear model predictive control (NMPC) and a multi-constraint fast solution algorithm combining the projection gradient method and augmented Lagrangian method, considering multiple constraints including phase plane stability, anti-sideslip, anti-rollover, and tire wear mitigation, improving the safety and stability of multi-axle distributed drive vehicles. To improve MPC real-time performance, researchers have proposed methods based on supervised learning: using input–output data generated by MPC to train neural networks (NNs) to achieve fast approximation of control strategies. This method has been successfully validated in benchmark chemical reactor models [25]. In the field of vehicle lateral stability control, researchers have further combined nonlinear autoregressive with exogenous inputs (NARX) neural networks with MPC, achieving control performance improvement, computation time reduction, and enhanced real-time deployment capability through two integration approaches [26]. However, the above research on multi-axle vehicles only utilized partial wheels in active wheel steering control, not fully exploiting the multi-degrees-of-freedom advantages of distributed drive vehicles.

Based on these challenges, integrated control of all-wheel steering (AWS) and direct yaw moment control (DYC) has emerged. All-wheel steering vehicles can independently control each wheel angle through electrical signals and complete torque distribution, providing a new steering platform for vehicle intelligence [27], while also changing the traditional single-input control mode of vehicles, making vehicle handling and stability control more precise and stable [28]. Chu et al. [29] transformed traditional wheel angle control into instantaneous center of rotation control, fully utilizing the advantages of all-wheel steering to solve tracking problems under large curvature turning conditions. Jneid et al. [30] proposed a regenerative braking torque vector control strategy considering both vehicle yaw rate and sideslip angle to improve vehicle stability. Gerardo Amato et al. [31] proposed a highly reconfigurable adaptive nonmodel control method for distributed drive electric vehicles. By performing slip vector allocation given longitudinal force, yaw moment requirements, and weight matrices, desired slip ratios are provided for each wheel, minimizing the total slip vector norm and keeping tires within the linear region to improve vehicle safety and stability. It can be seen that multi-objective integrated chassis control has become the mainstream trend in distributed drive vehicle control. In the application of distributed drive forms in heavy-duty vehicles, due to the large vehicle mass and body moment of inertia, the power demand for in-wheel motors during stability control is much greater than that of general passenger vehicles. To reduce the power requirements of in-wheel motors in multi-axle distributed drive heavy-duty vehicles, fully leverage the advantages of distributed drive configurations, and develop AWS/DYC coordinated control strategies that can effectively reduce peak torque, it is crucial to design targeted integrated control technology for all-wheel steering and yaw moment.

Based on this, this paper proposes a hierarchical stability control architecture for multi-axle special vehicles that integrates multi-variable coordinated control with drive–brake–steer decoupling control, employing DYC and AWS control methods. The upper layer utilizes MPC's characteristics of coordinating multiple state and control variables to reasonably adjust each control output, with a fuzzy controller dynamically adjusting MPC control weights. An MPC-supervised neural network controller (NN-MPC) is obtained by training neural networks using vehicle states and MPC control data as samples, improving control real-time performance, while a PID controller is designed for speed control. The lower-layer controller accomplishes precise allocation of control variables with the objective of optimizing tire load utilization. Finally, the effectiveness of the proposed method is verified on the Simulink/TruckSim co-simulation platform.

Different from existing research, the innovations of this paper are as follows:

1. A control-oriented linear parameter varying (LPV) tire model is introduced, improving the specificity of control algorithm research for multi-axle distributed special vehicles in practical application scenarios, especially under nonlinear conditions.
2. A hierarchical stability control architecture for multi-axle special vehicles integrating multi-variable coordinated control with drive–brake–steer decoupling control is proposed, significantly improving control precision.
3. The proposed neural network controller based on model predictive control effectively improves the real-time performance of handling stability control for multi-axle distributed heavy-duty vehicles.

The remainder of this paper is organized as follows: In Section 2, the vehicle's TruckSim model and 3-DOF model are established, and the model accuracy is verified. Section 3 designs the hierarchical stability controller. Section 4 conducts high-speed simulation verification and real vehicle verification. Section 5 concludes this paper and outlines future research work.

2. Dynamics Model of Multi-Axle Distributed Drive Vehicle

The establishment of vehicle dynamics models is the foundation for vehicle motion analysis and subsequent control strategy research. Addressing the structure and control requirements of the five-axle distributed drive test platform, this section establishes two dynamics models that are complementary in terms of fidelity and control applications: a high-fidelity vehicle model is constructed based on TruckSim, with its accuracy verified through real vehicle data; a three-degrees-of-freedom simplified model focusing on longitudinal, lateral, and yaw motions is derived to meet the real-time performance and analytical requirements of control algorithms. On this basis, a TruckSim/Simulink co-simulation environment is established, achieving a development closed-loop from simplified model algorithm design to high-fidelity model verification, enhancing development efficiency while ensuring theoretical rigor and laying the foundation for real vehicle testing.

2.1. TruckSim Vehicle Model

The research object of this paper is a distributed drive carrier test platform, which adopts a five-axle ten-wheel configuration. Compared with traditional multi-axle vehicles, the most significant features of this experimental platform are that it uses lithium-ion power battery packs as the energy system, with each wheel equipped with independent in-wheel motors and steering actuators, achieving complete decoupling control of driving, braking, and steering, specifically designed for algorithm development and verification of distributed drive configuration vehicles. The overall configuration of the test platform is shown in Figure 1.

Figure 1. Distributed drive carrier experimental platform.

The main parameters of the platform are shown in Table 1:

Table 1. Main parameters of the vehicle model.

Parameter	Value	Unit	Parameter	Value	Unit
Mass	1450.00	kg	Height of center of gravity	0.57	m
Length	5.60	m	Distance from CG to axle 1	2	m
Width	1.79	m	Distance from axle 2 to axle 1	1	m
Height	2.20	m	Distance from axle 3 to axle 1	2	m
Moment of inertia around x-axis	990.50	$kg \cdot m^2$	Distance from axle 4 to axle 1	3	m
Moment of inertia around y-axis	4136.40	$kg \cdot m^2$	Distance from axle 5 to axle 1	4	m
Moment of inertia around z-axis	3857.20	$kg \cdot m^2$			

Based on the main parameters of this platform, a high-fidelity vehicle model is established in TruckSim, with the power connections between the engine, transmission, and

https://doi.org/10.3390/vehicles8020026

differentials of each axle disconnected. Torque is directly applied to each wheel to simulate the working state of in-wheel motors. The established TruckSim model is shown in Figure 2.

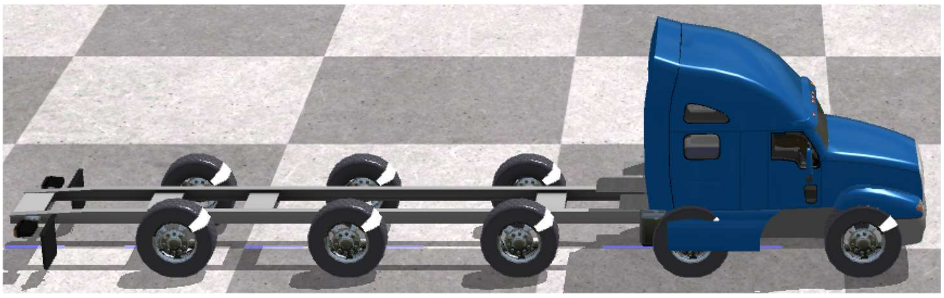

Figure 2. TruckSim model of the distributed drive carrier experimental platform.

To verify the accuracy and credibility of the TruckSim dynamics model, real vehicle road tests and simulation tests are conducted, respectively. The model and real vehicle are controlled to operate under the same speed and conditions. By comparing the consistency of key motion state parameters between them, it ensures that the model can accurately reflect the dynamic response characteristics of the actual vehicle. This platform integrates multiple sets of high-precision sensors, specifically including steering wheel angle sensors, vehicle body attitude sensors (capable of collecting signals such as yaw rate and lateral acceleration), pedal force sensors, sensors to measure tire steering angle, and tire vertical force sensors. Data from each sensor is transmitted in real time to the onboard data recorder via CAN bus protocol and then collected and stored by the host computer through a USB interface, ensuring the integrity and synchronization of test data. The connection architecture diagram of the test equipment is shown in Figure 3.

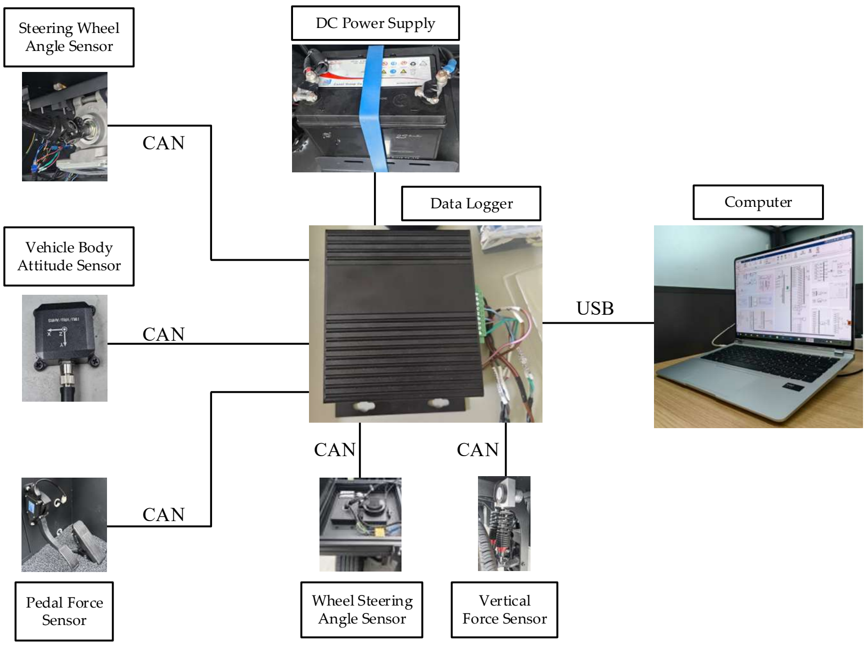

Figure 3. Connection architecture diagram of the experimental equipment.

Model validation tests are mainly completed through the trajectory reconstruction method. First, real vehicle dynamic performance tests are conducted on a predetermined test site, recording complete operational data of the vehicle under various complex conditions such as typical steering, acceleration, and braking. Subsequently, representative segments with significant dynamic responses are selected from the collected data, from which detailed road profile information is extracted, covering longitudinal slope, lateral superelevation, and three-dimensional spatial coordinates. The road profile information and vehicle speed information are imported into TruckSim to ensure strict consistency between the simulated vehicle and real vehicle tests in terms of longitudinal motion input. The test comparison results are shown in Figures 4–7. The yaw rate is directly measured by the IMU inertial measurement unit, and the sideslip angle is calculated from data measured by the onboard GPS and IMU:

$$\beta = \frac{-v_N \sin\psi - v_E \cos\psi}{v_N \cos\psi - v_E \sin\psi} \tag{1}$$

where $v_N = v_{GPS}\cos\varphi$ and $v_E = v_{GPS}\sin\varphi$ are the northward and eastward velocities of the vehicle in the geographic coordinate system, respectively; v_{GPS} is the ground speed measured by the onboard GPS; φ is the heading angle measured by the onboard GPS; and ψ is the yaw angle measured by the IMU.

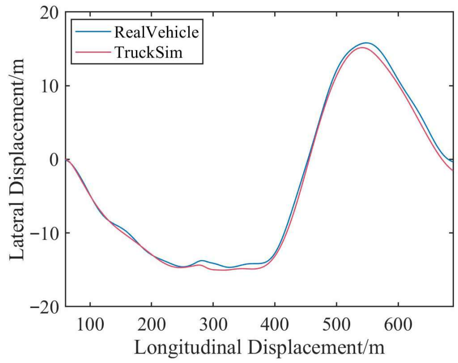

Figure 4. Comparison of motion trajectories.

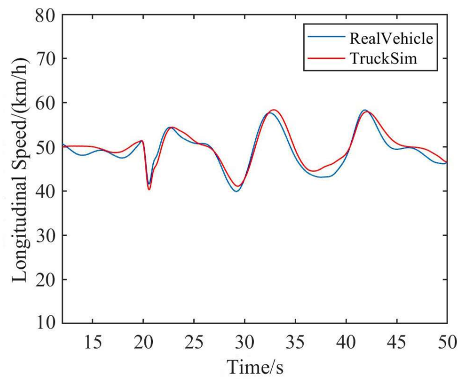

Figure 5. Comparison of longitudinal velocity.

Figures 4 and 5 show the driving trajectory and vehicle speed comparisons between real vehicle tests and the TruckSim simulation model under the same input conditions, respectively. From the comparison results, the maximum relative error of lateral position is 5.8%, and the maximum relative error of longitudinal vehicle speed is 6.5%, indicating that the simulation model reproduces well the path-tracking behavior of the real vehicle, providing a foundation for subsequent dynamics state comparisons.

Figures 5–7 present time-domain response comparisons of three important dynamics parameters: longitudinal vehicle speed, yaw rate, and sideslip angle. It can be seen that the longitudinal vehicle speed variation trends between the simulation and real vehicle are basically consistent, with main fluctuation amplitudes and phases also relatively well matched. In terms of yaw dynamics, due to factors such as the inability to perfectly align real vehicle sensor installation positions with the center of mass, test environment fluctuations, and driver operation differences, there are certain discrepancies between the yaw rate and sideslip angle curves output by TruckSim and the measured results. However, the overall variation trends are consistent, with average relative errors below 9%, mainly originating from sensor measurement noise, tire model parameter errors, and road adhesion coefficient errors, which are within acceptable ranges. The model reflects well the yaw motion characteristics of the real vehicle, with both the peak errors and phase lag of the yaw rate within reasonable engineering ranges. As a key indicator for evaluating vehicle stability, the simulated values of sideslip angle match well with the experimental data, particularly evident during transient response phases.

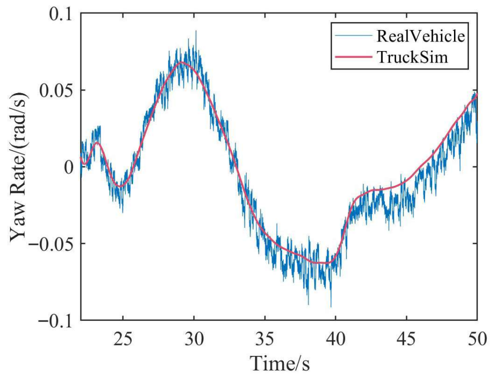

Figure 6. Comparison of yaw rate.

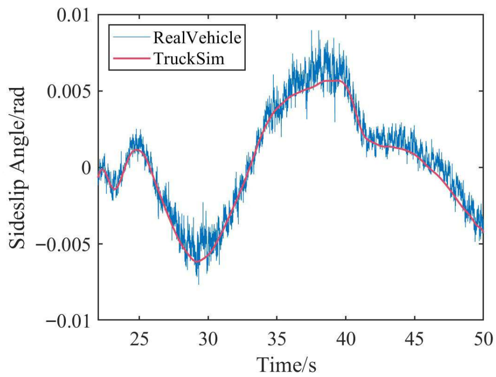

Figure 7. Comparison of sideslip angle at the center of gravity.

It should be noted that the vehicle yaw rate and sideslip angle signals are relatively noisy. In the control strategy design discussed below, a first-order low-pass filter is used to process these signals to obtain reference signals suitable for control.

Overall, the established TruckSim model can accurately reproduce the dynamic behavior of the real vehicle under both steady-state and transient conditions, with good consistency between model outputs and real vehicle test data. The results indicate that this simulation model is effective and reliable and can be used for subsequent control strategy development and verification.

2.2. Three-Degrees-of-Freedom Vehicle Model

To study the yaw stability of five-axle distributed drive vehicles, a three-degrees-of-freedom vehicle dynamics model containing longitudinal, lateral, and yaw motions is established, neglecting the effects of steering system stiffness and delay, the suspension system, and air resistance on the vehicle, as shown in Figure 8.

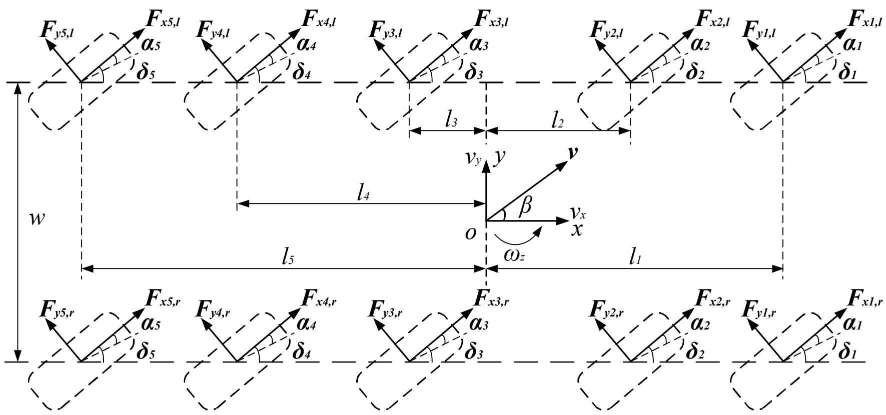

Figure 8. Three-degrees-of-freedom model of five-axle vehicle.

In the figure, oxy is the body-fixed coordinate system, with point o located at the vehicle's center of mass, the x-axis pointing toward the vehicle's longitudinal forward direction, and the y-axis pointing toward the vehicle's lateral left side. v is the actual velocity at the vehicle's center of mass; v_x and v_y are the component velocities of the actual velocity along the x-axis (longitudinal) and y-axis (lateral); $\delta_i(i = 1, 2, 3, 4, 5)$ represents the steering angles of wheels from axle one to five; α_i represents the sideslip angles of wheels from axle one to five, where it is assumed that wheels on the same axle have equal steering angles and sideslip angles; and l_i represents the distances from axles one to five to the vehicle's center of mass. Since the vehicle's center of mass is between the second and third axles, for convenience in subsequent formula derivation, l_1 and l_2 are defined as positive values, while l_3, l_4, and l_5 are negative values. w is the vehicle width; $F_{yi,l}$ and $F_{yi,r}$ are the lateral forces of the left and right wheels of axles one to five, respectively; $F_{xi,l}$ and $F_{xi,r}$ are the longitudinal forces of the left and right wheels of axles one to five, respectively; ω_z is the yaw rate of the vehicle around its center of mass; and β is the sideslip angle.

The vehicle longitudinal dynamics equation is

$$m(\dot{v}_x - v_y\omega_z) = \sum_{i=1}^{5} (F_{xi} \cdot \cos\delta_i - F_{yi} \cdot \sin\delta_i) \tag{2}$$

The vehicle lateral dynamics equation is

$$mv_x(\dot{\beta} + \omega_z) = \sum_{i=1}^{5} (F_{xi} \cdot \sin\delta_i + F_{yi} \cdot \cos\delta_i) \tag{3}$$

The vehicle yaw dynamics equation is

$$\begin{aligned} I_z\dot{\omega}_z = {} & \frac{w}{2} \cdot \sum_{i=1}^{5} (F_{xi,r} \cdot \cos\delta_i + F_{yi,r} \cdot \sin\delta_i) \\ & - \frac{w}{2} \cdot \sum_{i=1}^{5} (F_{xi,l} \cdot \cos\delta_i + F_{yi,l} \cdot \sin\delta_i) \\ & + \sum_{i=1}^{5} l_i \cdot (F_{yi} \cdot \cos\delta_i + F_{xi} \cdot \sin\delta_i) \end{aligned} \tag{4}$$

where $F_{xi} = F_{xi,l} + F_{xi,r}$ is the combined longitudinal force of the left and right wheels on the i-th axle; $F_{yi} = F_{yi,l} + F_{yi,r}$ is the combined lateral force of the left and right wheels on the i-th axle; m is the total vehicle mass; I_z is the vehicle's yaw moment of inertia; and ω_z and β are the vehicle yaw rate and sideslip angle, respectively.

When the vehicle's forward velocity v_x along the x-axis remains constant, the vehicle has only two degrees of freedom: lateral motion along the y-axis and yaw motion around the z-axis. Combined with the simplifying assumptions in this section, the actual vehicle is simplified into a two-degrees-of-freedom vehicle model supported on the ground by tires with lateral elasticity and having lateral and yaw motions. Equations (3) and (4) can be simplified into two-degrees-of-freedom dynamics equations characterizing vehicle lateral–yaw motion:

$$\begin{cases} m(\dot{v}_y + \omega_z v_x) = \sum_1^5 F_{yi} \\ I_z \dot{\omega}_z = \sum_1^5 F_{yi} l_i \end{cases} \tag{5}$$

The accuracy of the vehicle dynamics model largely depends on the precision of tire lateral force estimation. Particularly for multi-axle, heavy-duty vehicles performing special tasks, although the number of wheels increases, the vertical force on each wheel still reaches 5–10 times that of ordinary passenger cars. Under high-speed conditions, tire lateral force characteristics easily enter the saturation region. In the field of vehicle stability control, most scholars use linear tire models $F_y = \widetilde{C}_\alpha \alpha$ to estimate tire lateral forces. This model can calculate tire lateral forces well in regions with small tire sideslip angles and simplifies the overall vehicle model, improving controller computational efficiency. However, when the tire sideslip angle exceeds 5°, and the tire lateral force enters the saturation region, the calculation error of the linear tire model increases rapidly, leading to overall vehicle model mismatch. To improve the calculation accuracy of tire lateral forces, H. Dahmani et al. [32] proposed the Takagi–Sugeno tire model, which is significantly superior to the linear tire model in tire force calculation accuracy but still has obvious limitations. Actual tire dynamics characteristics are influenced by the combined effects of multiple factors including sideslip angle, slip ratio, road adhesion coefficient, and vertical load, while this model only considers the effect of sideslip angle. When vehicle load transfer occurs or road conditions change, the single-parameter Takagi–Sugeno model will produce large prediction errors, affecting control accuracy.

To overcome the shortcomings of the above models, Shi et al. [33] made systematic improvements based on the Takagi–Sugeno model and proposed a control-oriented linear parameter varying (LPV) tire model. This model represents tire cornering stiffness as a multi-variable function of sideslip angle, slip ratio, road adhesion coefficient, and vertical load, achieving an accurate description of tire characteristics under all operating conditions through parameter scheduling. The LPV tire model retains the advantages of linear structure convenient for controller design while accurately reflecting the nonlinear characteristics and parameter time-varying features of tires, providing an ideal modeling framework for high-performance vehicle stability control. Its expression is

$$F_y = \frac{F_z}{F_{z0}}(C_{y1}\omega_{y1} + C_{y2}\omega_{y2})\delta_y \tag{6}$$

where

$$\begin{cases} \sum_{i=1}^{2} \omega_{yi} = 1, 0 \le \omega_{yi} \le 1, \omega_{yi} = \dfrac{\theta_{yi}}{\theta_{y1} + \theta_{y2}} \\ \theta_{yi} = \dfrac{1}{(1 + \dfrac{\hat{\delta} - c_i}{a_i})^{2b_i}}, i = 1, 2 \\ \delta_y = \dfrac{\alpha}{1+\kappa}, \delta_x = \dfrac{\kappa}{1+\kappa}, \delta = \sqrt{\delta_y^2 + \delta_x^2}, \hat{\delta} = \dfrac{\mu_0 \delta}{\mu} \end{cases} \tag{7}$$

In Equations (6) and (7), a_i, b_i, c_i, C_{y1}, and C_{y2} are parameters to be identified; κ is the slip ratio; F_z is the vertical load; F_{z0} is the nominal load; μ is the friction coefficient and μ_0 is the nominal friction coefficient.

TruckSim 2019.0 incorporates a built-in parametric tabular tire model. This model calculates tire lateral forces under arbitrary operating conditions through two-dimensional interpolation of discrete lateral force and slip angle data at various vertical load levels. The model accurately captures the nonlinear cornering characteristics and force saturation behavior of tires under different loads. The software also provides a "Tire Tester" function for testing tire lateral force outputs under different combinations of slip angle, road friction coefficient, vertical load, and longitudinal slip ratio. The test vehicle is equipped with "175/65 R14" tires, and tire characteristic parameters of the corresponding specification from the TruckSim built-in tire database are employed in the simulation.

To accurately obtain the parameters of the LPV tire model, this paper designed systematic tire mechanical characteristic tests based on TruckSim tire experiments. The tire sideslip angle ranges from $-10°$ to $10°$ with an increment of $1°$, the road adhesion coefficient ranges from 0.6 to 1.0 with an increment of 0.2, the vertical load ranges from 500 N to 3000 N with an increment of 500 N, and the longitudinal slip ratio ranges from -0.1 to 0.1 with an increment of 0.05. These ranges can cover the working range of the studied vehicle.

Tire test data was obtained through batch simulation using TruckSim's Batch Matrix module, and the LPV tire model parameters were identified using the nonlinear least squares method. The results are shown in Table 2.

Table 2. LPV tire model parameter identification results.

Symbol	Value	Symbol	Value
a_1	-559.1639	a_2	0.20707
b_1	-1196.0384	b_2	-0.96037
c_1	0.35075	c_2	0.15964
C_{y1}	$-704{,}546.5483$	C_{y2}	-8.8127

The vehicle studied in this paper has a curb weight of 1450 kg and a rated payload of 500 kg, with each tire bearing a vertical load of approximately 1900 N under normal operating conditions. To verify the accuracy advantage of the LPV tire model under actual operating conditions, the tire slip characteristics data at a vertical load of 1961.33 N (closest to actual operating conditions) from TruckSim was selected as the reference benchmark. Figure 9 compares the tire lateral forces calculated by the linear tire model and the LPV tire model with the tire lateral force data provided by TruckSim under this vertical load condition.

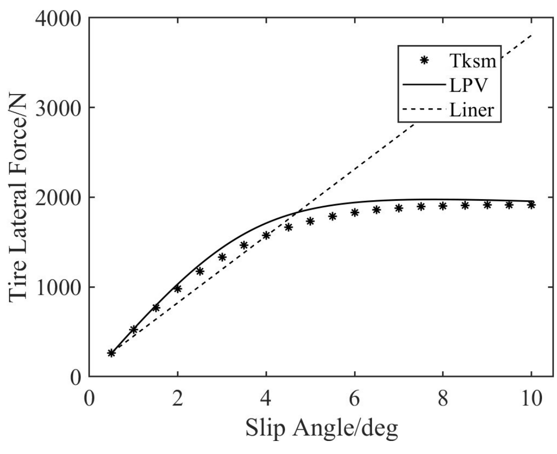

Figure 9. Comparison of tire lateral force.

As shown in Figure 9, the error between the lateral force calculated by the linear tire model and the standard data increases dramatically as the slip angle increases, with the error becoming particularly significant when the slip angle exceeds 5°. In contrast, the LPV tire model fits well with the standard data provided by TruckSim, maintaining high accuracy even after the lateral force curve enters the saturation region. Specifically, when the slip angle reaches 10°, the calculation error of the linear tire model reaches 62.47%, while the maximum error of the LPV tire model is only 8.4%, occurring at a slip angle of 4.5°. Under extreme conditions such as high-speed sharp turning, tire lateral force characteristics will significantly enter the saturation region, and the linear tire model will considerably overestimate the lateral force output, thereby affecting control system performance. The above comparison results demonstrate that the LPV tire model can accurately describe the nonlinear characteristics of tires. This significant accuracy improvement provides reliable theoretical model support for optimizing vehicle stability control system design and helps improve the accuracy and robustness of control algorithms.

Substituting the LPV tire model shown in Equation (6) into the vehicle lateral dynamics in Equation (5), the enhanced vehicle model considering tire nonlinear characteristics is obtained v_x:

$$\begin{cases} m(\dot{v}_y + \omega_z v_x) = \sum_1^5 2\zeta_i \alpha_i \\ I_z \dot{\omega}_z = \sum_1^5 2\zeta_i \alpha_i l_i \end{cases} \tag{8}$$

where

$$\begin{array}{l} \zeta_i = \frac{F_{zi}(C_{y1}\omega_{y1} + C_{y2}\omega_{y2})}{F_{z0}(1+\kappa_i)} \\ \alpha_i = -\left(\delta_i - \frac{v_y + l_i \omega_z}{v_x}\right) = \beta + \frac{l_i \omega_z}{v_x} - \delta_i \end{array} \tag{9}$$

In the equations, F_{zi} is the vertical load of the vehicle's i-th axle tire, and κ_i is the slip ratio of the i-th axle tire.

According to the Ackermann steering principle, when the vehicle maintains stable steering, the perpendicular lines from each wheel's rotation center perpendicular to the tire's neutral plane should converge at the same instantaneous center of rotation. The vehicle's instantaneous center of rotation O is located on the extension of the third axle wheel centerline, as shown in Figure 10.

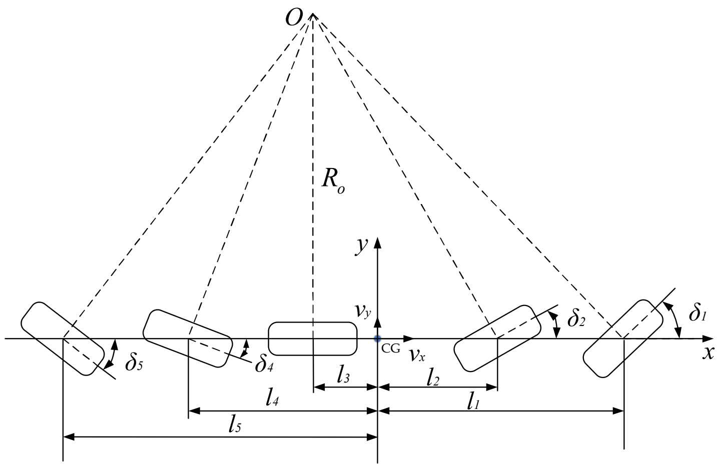

Figure 10. Ackermann steering model.

In Figure 10, R_o is the turning radius, and the steering angles of each vehicle axle satisfy the following geometric relationships:

$$\begin{cases} \tan\delta_1 = (l_1 + l_3)/R_o \\ \tan\delta_2 = (l_2 + l_3)/R_o \\ \tan\delta_4 = (l_4 - l_3)/R_o \\ \tan\delta_5 = (l_5 - l_3)/R_o \end{cases} \tag{10}$$

Based on the small angle input assumption, the relationships between the tire angles of axles 2, 4, and 5 and the first axle tire angle can be obtained as follows:

$$\begin{cases} \delta_2 = k_{12}\delta_1 \\ \delta_4 = k_{14}\delta_1 \\ \delta_5 = k_{15}\delta_1 \end{cases} \tag{11}$$

where $k_{12} = \frac{l_2+l_3}{l_1+l_3}, k_{14} = \frac{l_4-l_3}{l_1+l_3}, k_{15} = \frac{l_5-l_3}{l_1+l_3}$ are the steering angle gains of wheels on vehicle axles 2, 4, and 5 relative to the first axle wheel angle, respectively.

Substituting Equation (11) into Equation (8), the state-space equation for vehicle lateral dynamics is obtained:

$$\begin{bmatrix} \dot{\beta} \\ \dot{\omega}_z \end{bmatrix} = \begin{bmatrix} \frac{2\sum\limits_{i=1}^{5}\zeta_i}{mv_x} & \frac{2\sum\limits_{i=1}^{5}\zeta_i l_i}{mv_x^2} - 1 \\ \frac{2\sum\limits_{i=1}^{5}\zeta_i l_i}{I_z} & \frac{2\sum\limits_{i=1}^{5}\zeta_i l_i^2}{I_z v_x} \end{bmatrix} \begin{bmatrix} \beta \\ \omega_z \end{bmatrix} + \begin{bmatrix} \frac{-2(\zeta_1 + \zeta_2 k_{12} + \zeta_4 k_{14} + \zeta_5 k_{15})}{mv_x} \\ \frac{-2(\zeta_1 l_1 + \zeta_2 k_{12} l_2 + \zeta_4 k_{14} l_4 + \zeta_5 k_{15} l_5)}{I_z} \end{bmatrix} [\delta_1] \tag{12}$$

2.3. Stability Control Objectives

In vehicle-handling stability control research, three state variables are primarily focused on: longitudinal vehicle speed v_x, yaw rate ω_z, and sideslip angle β.

The control target for vehicle speed $v_{x,des}$ is mainly determined by the driver's intention. The desired value for vehicle yaw rate $\omega_{z,des}$ is determined by the gain of the first steering axle with respect to yaw rate obtained from the vehicle's two-degrees-of-freedom model and the maximum road adhesion force.

Applying Laplace transform to both sides of Equation (12) with initial conditions set to zero, the transfer functions of sideslip angle β and yaw rate ω_z with respect to the first axle wheel angle δ_1 are obtained:

$$\begin{bmatrix} \frac{\beta(s)}{\delta_1(s)} \\ \frac{\omega_z(s)}{\delta_1(s)} \end{bmatrix} = \frac{a \cdot \mathrm{b}}{s^2 - cs + d} \tag{13}$$

where

$$\begin{cases} a = \begin{bmatrix} s - \frac{2\sum\limits_{i=1}^{5}\zeta_i l_i^2}{I_z v_x} & \frac{2\sum\limits_{i=1}^{5}\zeta_i l_i}{mv_x^2} - 1 \\ \frac{2\sum\limits_{i=1}^{5}\zeta_i l_i}{I_z} & s - \frac{2\sum\limits_{i=1}^{5}\zeta_i}{mv_x} \end{bmatrix} \\ b = \begin{bmatrix} \frac{-2(\zeta_1 + \zeta_2 k_{12} + \zeta_4 k_{14} + \zeta_5 k_{15})}{mv_x} \\ \frac{-2(\zeta_1 l_1 + \zeta_2 k_{12} l_2 + \zeta_4 k_{14} l_4 + \zeta_5 k_{15} l_5)}{I_z} \end{bmatrix} \\ c = \frac{2I_z \sum\limits_{i=1}^{5}\zeta_i + 2m\sum\limits_{i=1}^{5}\zeta_i l_i^2}{I_z m v_x} \\ d = \frac{4\sum\limits_{i=1}^{5}\zeta_i \sum\limits_{i=1}^{5}\zeta_i l_i^2 - (2\sum\limits_{i=1}^{5}\zeta_i l_i)^2 + 2mv_x^2 \sum\limits_{i=1}^{5}\zeta_i l_i}{I_z m v_x^2} \end{cases} \tag{14}$$

From Equation (13), the steady-state gain $G_{\omega_z ss}$ of yaw rate with respect to the first axle wheel angle can be obtained:

$$G_{\omega_z ss} = \left.\frac{\omega_z(s)}{\delta_1(s)}\right|_{s=0} = \frac{v_x/L_e}{1 + v_x^2 \cdot K} \tag{15}$$

where K is the stability factor, and L_e is the equivalent wheelbase coefficient:

$$K = \frac{2m\sum_1^5 \zeta_i l_i}{4\sum_{i=1}^{5} \zeta_i \sum_{i=1}^{5} \zeta_i l_i^2 - (2\sum_{i=1}^{5} \zeta_i l_i)^2} \tag{16}$$

$$L_e = \frac{4\sum_{i=1}^{5} \zeta_i \sum_{i=1}^{5} \zeta_i l_i^2 - (2\sum_{i=1}^{5} \zeta_i l_i)^2}{2b\sum_{i=1}^{5} \zeta_i - 2a\sum_{i=1}^{5} \zeta_i l_i} \tag{17}$$

$$a = 2(\xi_1 + \xi_2 k_{12} + \xi_4 k_{14} + \xi_5 k_{15}) \tag{18}$$

$$b = 2(\xi_1 l_1 + \xi_2 l_2 k_{12} + \xi_4 l_4 \mathrm{k}_{14} + \xi_5 l_5 k_{15}) \tag{19}$$

The vehicle's desired yaw rate equals the product of the yaw rate steady-state gain and the first axle wheel angle:

$$\omega_{z,des} = G_{\omega_z ss} \cdot \delta_1 = \frac{v_x}{L_e(1 + v_x^2 \cdot K)} \cdot \delta_1 \tag{20}$$

Additionally, the vehicle's desired yaw rate should satisfy the constraint on vehicle lateral acceleration imposed by the road friction coefficient:

$$|\omega_{z,des}| \le \frac{\mu \cdot g}{v_x} \tag{21}$$

where μ is the road friction coefficient, and g is the gravitational acceleration.

Therefore, the vehicle's desired yaw rate is

$$\omega_{z,des} = \min\left(\left|\frac{v_x \delta_1}{L_e(1 + v_x^2 \cdot K)}\right|, \left|\frac{\mu \cdot g}{v_x}\right|\right)\mathrm{sgn}\delta_1 \tag{22}$$

The determination of the vehicle's ideal sideslip angle β_{des} can also adopt the calculation method of multiplying steady-state response characteristics by the steering wheel angle. However, in engineering practice, this parameter is often set to zero, and this study similarly sets the target sideslip angle to zero.

3. Hierarchical Controller Design

Based on the characteristics that each wheel of distributed drive vehicles can be independently driven, braked, and steered, this paper adopts direct yaw moment and all-wheel steering strategies, selects PID control and MPC control for controller design, and proposes a hierarchical stability control architecture, as shown in Figure 11. The specific descriptions are as follows:

(1) Control objective module: The two-degrees-of-freedom model calculates the current vehicle's ideal yaw rate based on the front-wheel steering angle input, outputs the desired longitudinal vehicle speed according to the driver's intention, and outputs 0 for the desired sideslip angle;

(2) In the upper-level controller, the PID speed control module calculates the longitudinal resultant force F_{xa} required to track the longitudinal vehicle speed $v_{x,des}$. The MPC

controller calculates the required additional yaw moment ΔM_z and wheel angles δ_2, δ_3, δ_4, δ_5 for each axle based on the input ideal yaw rate $\omega_{z,des}$ and sideslip angle β_{des}. The fuzzy controller dynamically adjusts the control weights of the MPC controller based on the output wheel angles;

(3) The lower-level controller, targeting optimal tire adhesion utilization rate, distributes the longitudinal resultant force, additional yaw moment, and axle angles transmitted from the upper-level controller into driving and braking torques and active steering angles for each wheel;

(4) The vehicle dynamics model receives the control quantities output from the lower-level controller and executes them, while transmitting vehicle states such as real-time longitudinal vehicle speed, yaw rate, sideslip angle, and wheel angles to the control objective calculation module and upper- and lower-level controllers.

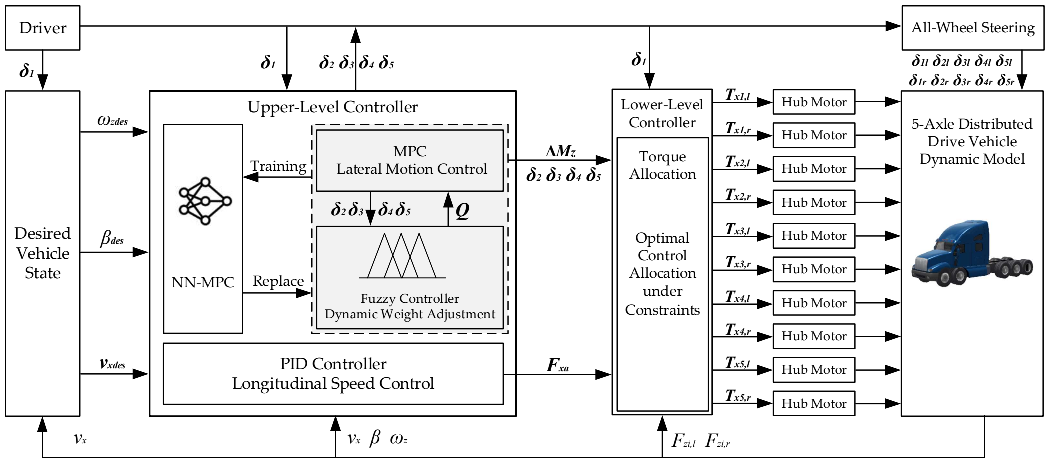

Figure 11. Hierarchical stability control architecture for five-axle vehicle.

Due to the large number of variables to be optimized in the MPC controller for multi-axle distributed drive vehicles, resulting in poor real-time performance and difficulty in meeting the fast response requirements of practical engineering applications, this paper uses neural network methods to approximate and replace the MPC control law, significantly improving the controller's online computational efficiency through "replacing optimization with learning". First, simulations are conducted using the MPC controller under various operating conditions, collecting data on different vehicle states and corresponding MPC control quantities, including normal conditions and extreme scenarios with added disturbances to enhance the diversity and generalization capability of training samples. Based on this, a neural network controller is constructed and supervised training is performed with the large sample data. The trained neural network replaces the MPC controller while ensuring control accuracy and system stability.

Regarding vehicle dynamics stability criteria and control intervention mechanism research, existing methods generally establish stability partition models based on the $\beta - \dot{\beta}$ phase plane method, implementing segmented control strategies based on state identification by constructing vehicle state stability regions, critical regions, and instability regions. However, for the dynamic characteristics of multi-axle, heavy-duty vehicles under high-speed sharp-turning conditions, traditional partition control strategies are prone to control hysteresis and state-jumping problems due to sudden changes in phase plane boundary conditions. Therefore, this study adopts a full-domain continuous control strategy, implementing real-time feedback control under all conditions, enabling the vehicle to track desired states in real time to ensure overall system stability.

3.1. Upper-Level Controller

Direct yaw moment and all-wheel steering strategies are adopted for vehicle lateral motion control. Since the first axle angle is used to calculate the ideal yaw rate and to avoid affecting the driver's vehicle trajectory tracking capability, the first axle active steering angle is not controlled. Therefore, the model predictive controller's input is $u = \begin{bmatrix} \delta_2 & \delta_3 & \delta_4 & \delta_5 & \Delta M_z \end{bmatrix}^{\mathrm{T}}$, and the output is the vehicle state $x = \begin{bmatrix} \beta & \omega_z \end{bmatrix}^{\mathrm{T}}$. Adding the controller quantities to Equation (12), the control system state equation is obtained:

$$
\begin{aligned}
\begin{bmatrix} \dot{\beta} \\ \dot{\omega}_z \end{bmatrix} = & \begin{bmatrix} \frac{2\sum\limits_{i=1}^{5}\zeta_i}{m\boldsymbol{v_x}} & \frac{2\sum\limits_{i=1}^{5}\zeta_i l_i}{m\boldsymbol{v_x^2}} - 1 \\ \frac{2\sum\limits_{i=1}^{5}\zeta_i l_i}{I_z} & \frac{2\sum\limits_{i=1}^{5}\zeta_i l_i^2}{I_z v_x} \end{bmatrix} \begin{bmatrix} \beta \\ \omega_z \end{bmatrix} + \begin{bmatrix} \frac{-2\zeta_2}{mv_x} & \frac{-2\zeta_3}{mv_x} & \frac{-2\zeta_4}{mv_x} & \frac{-2\zeta_5}{mv_x} & 0 \\ \frac{2\zeta_2 l_2}{I_z} & \frac{2\zeta_3 l_3}{I_z} & \frac{2\zeta_4 l_4}{I_z} & \frac{2\zeta_5 l_5}{I_z} & \frac{1}{I_z} \end{bmatrix} \begin{bmatrix} \delta_2 \\ \delta_3 \\ \delta_4 \\ \delta_5 \\ \Delta M_z \end{bmatrix} \\
& + \begin{bmatrix} \frac{-2(\zeta_1 + \zeta_2 k_{12} + \zeta_4 k_{14} + \zeta_5 k_{15})}{m\boldsymbol{v_x}} \\ \frac{-2(\zeta_1 l_1 + \zeta_2 k_{12} l_2 + \zeta_4 k_{14} l_4 + \zeta_5 k_{15} l_5)}{I_z} \end{bmatrix} \delta_1
\end{aligned} \tag{23}
$$

Rewriting it in standard state-space equation form:

$$
\begin{cases} \dot{x} = Ax + Bu + C \\ y = Dx \end{cases} \tag{24}
$$

where

$$
A = \begin{bmatrix} \frac{10C}{m\boldsymbol{v_x}} & \frac{2C\sum\limits_{i=1}^{5} l_i}{m\boldsymbol{v_x^2}} - 1 \\ \frac{2C\sum\limits_{i=1}^{5} l_i}{I_z} & \frac{2C\sum\limits_{i=1}^{5} l_i^2}{I_z \boldsymbol{v_x}} \end{bmatrix} x = \begin{bmatrix} \beta & \omega_z \end{bmatrix}^T B = \begin{bmatrix} \frac{-2C}{mv_x} & \frac{-2C}{mv_x} & \frac{-2C}{mv_x} & \frac{-2C}{mv_x} & 0 \\ \frac{2Cl_2}{I_z} & \frac{2Cl_3}{I_z} & \frac{2Cl_4}{I_z} & \frac{2Cl_5}{I_z} & \frac{1}{I_z} \end{bmatrix}
$$

$$
C = \begin{bmatrix} \frac{-2C}{mv_x} \\ \frac{-2Cl_1}{I_z} \end{bmatrix} \delta_1 \; y = \begin{bmatrix} \beta & \omega_z \end{bmatrix}^T D = diag(1,1)
$$

Using the forward Euler method to convert continuous state Equation (24) to a discrete equation:

$$
\begin{cases} x(k+1) = A_k x(k) + B_k u(k) + C_k \\ y(k) = Dx(k) \end{cases} \tag{25}
$$

where $A_k = I + T_s A$, $B_k = T_s B$, $C_k = T_s C$, T_s is the sampling time; $x(k)$ is the system's current state; $x(k+1)$ is the system's next state; and $u(k)$ is the system's current control quantity.

For the model predictive controller, within the prediction horizon, define $u(k+i|k)$ as the control quantity at time $k+i$ predicted at time k, and $x(k+i|k)$ as the state quantity when the system input is $u(k+i|k)$ at time $k+i$ predicted at time k.

Then, at time $k+1$:

$$
x(k+1|k) = Ax(k|k) + Bu(k|k) + C \tag{26}
$$

At time, $k+2$:

$$
\begin{aligned} x(k+2|k) &= Ax(k+1|k) + Bu(k+1|k) + C \\ &= A^2 x(k|k) + ABu(k|k) + AC + Bu(k+1|k) + C \end{aligned} \tag{27}
$$

At time $k+3$:

$$\begin{aligned} x(k+3|k) &= Ax(k+2|k) + Bu(k+2|k) + C \\ &= A^3x(k|k) + A^2Bu(k|k) + A^2C \\ &+ABu(k+1|k) + AC + u(k+2|k) + C \end{aligned} \tag{28}$$

At time $k+N$:

$$\begin{aligned} x(k+N|k) &= Ax(k+N-1|k) + Bu(k+N-1|k) + C \\ &= A^N x(k|k) + \textstyle\sum_0^{N-1} A^i Bu(k+i|k) + \textstyle\sum_0^{N-1} A^i C \end{aligned} \tag{29}$$

Writing the above iterative process in matrix form:

$$\begin{bmatrix} x(k+1|k) \\ x(k+2|k) \\ \vdots \\ x(k+N|k) \end{bmatrix} = \begin{bmatrix} A \\ A^2 \\ \vdots \\ A^N \end{bmatrix} x(k|k) + \begin{bmatrix} C \\ AC+C \\ \vdots \\ \sum_0^{N-1} A^i C \end{bmatrix} + \begin{bmatrix} B & 0 & 0 & \cdots & 0 \\ AB & B & 0 & \cdots & 0 \\ A^2B & AB & B & \cdots & 0 \\ \vdots & \vdots & \vdots & \vdots & \vdots \\ A^{N-1}B & A^{N-2}B & A^{N-3}B & \cdots & B \end{bmatrix} \begin{bmatrix} u(k|k) \\ u(k+1|k) \\ \vdots \\ u(k+N-1|k) \end{bmatrix} \tag{30}$$

Rewriting in compact form:

$$X(k) = \Phi x(k|k) + \Gamma U(k) + Y \tag{31}$$

where

$$X(k) = \begin{bmatrix} x(k+1|k) \\ x(k+2|k) \\ \vdots \\ x(k+N|k) \end{bmatrix} \Phi = \begin{bmatrix} A \\ A^2 \\ \vdots \\ A^N \end{bmatrix} \Gamma = \begin{bmatrix} B & 0 & 0 & \cdots & 0 \\ AB & B & 0 & \cdots & 0 \\ A^2B & AB & B & \cdots & 0 \\ \vdots & \vdots & \vdots & \vdots & \vdots \\ A^{N-1}B & A^{N-2}B & A^{N-3}B & \cdots & B \end{bmatrix}$$

$$U(k) = \begin{bmatrix} u(k|k) \\ u(k+1|k) \\ \vdots \\ u(k+N-1|k) \end{bmatrix} Y = \begin{bmatrix} C \\ AC+C \\ \vdots \\ \sum\limits_{i=0}^{N-1} A^i C \end{bmatrix}$$

$X(k)$ is all state variables within the prediction interval predicted at time k; $U(k)$ is the control quantity sequence calculated at time k; Φ and Γ are both coefficient matrices; and Y is a column vector related to the first axle angle. Here, it is assumed that the first axle angle remains unchanged within the control horizon, all taking the first axle angle δ_1 at time k.

The optimization objective function of the model predictive controller is defined as

$$J = \frac{1}{2} e^T(k+N_p|k) Se(k+N_p|k) + \frac{1}{2} \sum_{i=0}^{N_p-1} \begin{matrix} [e^T(k+i|k)Qe(k+i|k) \\ +u^T(k+i|k)Ru(k+i|k)] \end{matrix} \tag{32}$$

where N_p are the prediction and control steps; $e(k+N_p|k)$ is the difference between the system's desired state and current state at the last step in the prediction steps; and $e(k) = |X_d(k) - X(k)|$ is the difference between the system's desired state and current state. $Q = diag\begin{pmatrix} q_1 & q_2 \end{pmatrix}$, $R = diag\begin{pmatrix} r_1 & r_2 & r_3 & r_4 & r_5 \end{pmatrix}$, and $S = diag\begin{pmatrix} s_1 & s_2 \end{pmatrix}$ are the weight matrices for state quantities, control quantities, and terminal error, respectively. To ensure control system stability, the three weight matrices designed here are all greater than 0.

The optimization objective function should satisfy the following constraints:
Dynamic constraints:

$$\begin{cases} x(k+1) = A_k x(k) + B_k u(k) + C_k \\ y(k) = Dx(k) \end{cases} \tag{33}$$

Control variable constraints:

$$u_{\min}(k+i) \le u(k+i) \le u_{\max}(k+i) \qquad i = 0, 1, \cdots, N-1 \tag{34}$$

Output constraints:

$$y_{\min}(k+i) \le y(k+i) \le y_{\max}(k+i) \qquad i = 0, 1, \cdots, N-1 \tag{35}$$

To solve the MPC optimal control sequence, the performance index is converted to standard quadratic programming form. Substituting Equation (25) into Equation (32):

$$\begin{aligned} J = & \tfrac{1}{2}(x(k\,|\,k) - x_d(k\,|\,k))^T Q(x(k|k) - x_d(k|k)) \\ & + \tfrac{1}{2}(\Phi x(k\,|\,k) + \Gamma U(k) + Y - X_d(k))^T \Omega(\Phi x(k|k) \\ & + \Gamma U(k) + Y - X_d(k)) \ + \tfrac{1}{2} U^T(k) \Psi U(k) \end{aligned} \tag{36}$$

where $\Omega = \begin{bmatrix} Q & \cdots & 0 \\ \vdots & Q & \vdots \\ 0 & \cdots & S \end{bmatrix}$ and $\Psi = \begin{bmatrix} R & \cdots & 0 \\ \vdots & \ddots & \vdots \\ 0 & \cdots & R \end{bmatrix}$ are both $2N_p \times 2N_p$ matrices; Z is a scalar. The first term $\frac{1}{2}(x(k\,|\,k) - x_d(k\,|\,k))^T Q(x(k|k) - x_d(k|k))$ is determined by the initial state $x(k|k)$ and is not affected by the control quantity $U(k)$, so it can be ignored when performing optimization calculations:

$$J = \frac{1}{2} U^T[k](\Gamma^T \Omega \Gamma + \Psi) U[k] + U^T[k] \Gamma^T \Omega Z \tag{37}$$

Defining $F = \Gamma^{\mathrm{T}} \Omega Z$ and $H = \Gamma^{\mathrm{T}} \Omega \Gamma + \Psi$, the standard quadratic programming form is obtained:

$$J = U^T[k] F + \frac{1}{2} U^T[k] H U[k] \tag{38}$$

For the MPC controller's state variables $y(k+i) = \begin{bmatrix} \omega_z & \beta \end{bmatrix}^{\mathrm{T}}$, the yaw rate ω_z and sideslip angle β must satisfy the vehicle's stability boundaries:

$$\begin{cases} |\omega_z| < \frac{\mu g}{v_x} \\ |\beta| < \arctan(0.02\ \mu g) \end{cases} \tag{39}$$

Considering actuator output constraints, each in-wheel motor of distributed drive passenger cars can provide a maximum torque of 1000–1500 N · m. Although the research object in this paper is a 1.7 t distributed drive five-axle vehicle, the research goal aims to lay the foundation for future applications in heavy special vehicles with masses much greater than passenger cars (such as 50 t class). Although the lightweight vehicle itself and the multi-axle, multi-motor configuration can share the driving pressure to some extent, considering the huge driving torque required for heavy vehicles to track the ideal yaw rate under high-speed conditions, this study does not specifically limit the maximum driving torque that in-wheel motors can provide during the strategy design phase, only analyzing application possibilities in the simulation results. The range of additional yaw moment ΔM_z is taken as $[-\infty, +\infty]$. For active steering angle limits, vehicles with rear-wheel active steering function have steering angle ranges of 10°∼15°. This paper takes the active steering angle range for wheels on axles 2, 3, 4, and 5 as $[-10°, 10°]$. Therefore, the final value range of the model predictive controller's control quantities is $u_{\max} = \begin{bmatrix} 10° & 10° & 10° & 10° & +\infty \end{bmatrix}^{\mathrm{T}}$, $u_{\min} = \begin{bmatrix} -10° & -10° & -10° & -10° & -\infty \end{bmatrix}^{\mathrm{T}}$. The control sequence value range is $U_{\max}(k) = \begin{bmatrix} u_{\max} & \cdots & u_{\max} \end{bmatrix}^{\mathrm{T}}$, $U_{\min}(k) = \begin{bmatrix} u_{\min} & \cdots & u_{\min} \end{bmatrix}^{\mathrm{T}}$.

Representing this control problem as a standard quadratic programming problem:

$$\begin{cases} \min J = U^T[k]F + \frac{1}{2}U^T[k]HU[k] \\ \text{s.t} \begin{bmatrix} I \\ -I \end{bmatrix} U[k] \leq \begin{bmatrix} U_{\max}(k) \\ U_{\min}(k) \end{bmatrix} \end{cases} \tag{40}$$

This problem can be solved using the quadprog function in MATLAB R2023a. Thus, the optimal control input sequence $U(k)$ for the prediction interval at time k is obtained, and then the optimal control quantity $u(k)$ at time k is obtained.

To compare the control effect of this control strategy, a model predictive controller integrating active rear-wheel steering (vehicle 4th and 5th axle wheels) and direct yaw moment control is designed, with its control equation as

$$\begin{aligned} \begin{bmatrix} \dot{\beta} \\ \dot{\omega}_z \end{bmatrix} = & \begin{bmatrix} \frac{2\sum\limits_{i=1}^{5}\zeta_i}{mv_x} & \frac{2\sum\limits_{i=1}^{5}\zeta_i l_i}{mv_x^2} - 1 \\ \frac{2\sum\limits_{i=1}^{5}\zeta_i l_i}{I_z} & \frac{2\sum\limits_{i=1}^{5}\zeta_i l_i^2}{I_z v_x} \end{bmatrix} \begin{bmatrix} \beta \\ \omega_z \end{bmatrix} + \begin{bmatrix} \frac{-2\zeta_4}{mv_x} & \frac{-2\zeta_5}{mv_x} & 0 \\ \frac{2\zeta_4 l_4}{I_z} & \frac{2\zeta_5 l_5}{I_z} & \frac{1}{I_z} \end{bmatrix} \begin{bmatrix} \delta_4 \\ \delta_5 \\ \Delta M_z \end{bmatrix} \\ & + \begin{bmatrix} \frac{-2(\zeta_1 + \zeta_2 k_{12} + \zeta_4 k_{14} + \zeta_5 k_{15})}{mv_x} \\ \frac{-2(\zeta_1 l_1 + \zeta_2 k_{12} l_2 + \zeta_4 k_{14} l_4 + \zeta_5 k_{15} l_5)}{I_z} \end{bmatrix} \delta_1 \end{aligned} \tag{41}$$

The comparison controller is also implemented based on MPC control, with the derivation process consistent with the above and omitted here.

The active steering angles of each wheel output by the model predictive controller differ significantly, which leads to different wear degrees of wheels on each axle. Additionally, in the lower-level control, influenced by the tire adhesion ellipse, the larger the active steering angle, the smaller the longitudinal force component the tire can provide, thus affecting the controller's effectiveness [14,23]. The weights of various control quantities in the model predictive controller are not simple proportional relationships of each axle distance, making it difficult to pre-adjust. This paper adopts fuzzy control to dynamically adjust the model predictive controller weights, making the absolute values of active steering angles output by each wheel similar, thereby improving the control system's robustness. For the control object in this paper, the state variable weight values $Q = diag((100{,}000),\ 100)$ and terminal error weight values $S = diag(1,\ 1)$ are first determined through multiple simulation experiments, along with the initial control weight values $R = diag(0.05,\ 0.05,\ 0.05,\ 0.05,\ 0.000001)$. Then, a fuzzy controller is designed to adjust the first four items in weight R that determine the active steering angles of wheels on axles 2, 3, 4, and 5.

The fuzzy controller's input is the difference between the absolute value of the active steering angles of wheels on axles 2, 3, 4, and 5 and the average of the sum of absolute values of the active steering angles of all axle wheels $e_{\delta i}(i = 2, 3, 4, 5)$:

$$e_{\delta i} = |\delta_i| - \frac{\sum\limits_{i=2}^{5}|\delta_i|}{4} \tag{42}$$

Based on the output results of the MPC controller without dynamic weight adjustment, the universe of discourse for $e_{\delta i}$ is set as $(-0.1, 0.1)$, with fuzzy subsets divided into {NB (Negative Big), NS (Negative Small), Z (Zero), PS (Positive Small), PB (Positive Big)}.

The fuzzy controller's output is the adjustment amount $r_i(i = 1, 2, 3, 4)$ for the four active steering angle control weights of the model predictive controller. To avoid drastic fluctuations, the adjustment amount should be set relatively small; hence, its universe of discourse is set as $(-0.025, 0.025)$, with fuzzy subsets divided into {NB (Big Decrease), NS (Small Decrease), Z (Unchanged), PS (Small Increase), PB (Big Increase)}. When $e_{\delta i}$ is negative, it indicates that the corresponding control weight r_i is relatively large and should be decreased to increase the output of the corresponding axle's active steering angle and vice versa. Inputting the above rules into MATLAB's fuzzy control toolbox and applying centroid method defuzzification, the obtained weight adjustment rule output is shown in Figure 12.

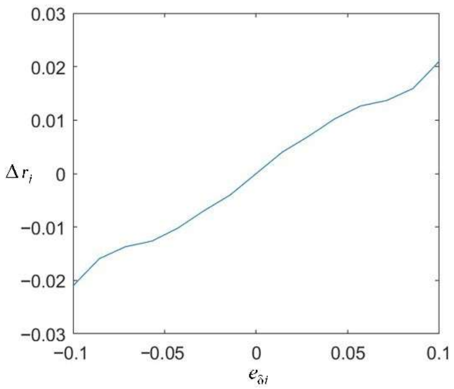

Figure 12. Weight adjustment rules.

A longitudinal vehicle speed PID controller is designed for speed control. The controller calculates the required longitudinal resultant force F_{xa} for the vehicle body. F_{xa} is composed of the force components of all wheels in the vehicle body's x-axis direction. Combining with the vehicle longitudinal dynamics in Equation (2) and neglecting external disturbances:

$$m(\dot{v}_x - v_y\omega_z) = F_{xa} - \sum_{i=1}^{5} F_{yi(l,r)} \cdot \sin\delta_i \tag{43}$$

This yields

$$F_{xa} = \mathrm{m}(\dot{v}_x - f_p) \tag{44}$$

where

$$f_p = -\frac{1}{\mathrm{m}}\sum_{i=1}^{5} F_{yi(l,r)} \cdot \sin\delta_i + v_y\omega_z \tag{45}$$

The PID controller's input is defined as the error signal of the vehicle's longitudinal speed:

$$e_{vx} = v_{xdes} - v_x \tag{46}$$

The designed control law is

$$F_{xa} = \mathrm{m}(k_p e_{vx} + k_i \int e_{vx} dt + k_d \frac{de_{vx}}{dt} - f_p) \tag{47}$$

where $k_p = 21.2$ is the proportional coefficient; $k_i = 8.3$ is the integral coefficient; and $k_d = 0.1$ is the derivative coefficient, with their values determined through multiple simulation experiments.

3.2. Lower-Level Controller

The lower-level controller reasonably distributes the additional yaw moment ΔM_z, active steering angles of vehicle axles 2, 3, 4, and 5, and vehicle body longitudinal resultant force F_{xa} calculated by the upper-level controller into active steering angles and driving and braking torques for each wheel. Considering the characteristics of high-speed large steering angle conditions, a coaxial equal angle distribution strategy is adopted, directly mapping the axle angles output by MPC to the dual wheels on the same axle. By moderately increasing the tire wear cost, priority is given to ensuring the vehicle's yaw stability and drive system energy consumption optimization. Based on this, a controller is designed with the optimization objective of minimizing the tire load rate of all wheels, obtaining the optimal torque for each wheel under control quantity constraints.

According to vehicle dynamics, the relationship between target control force (moment) and tire longitudinal force is

$$\tau = B \cdot u \tag{48}$$

where τ is the target control force (moment):

$$\tau = \begin{bmatrix} F_{xa} & \Delta M_z \end{bmatrix}^T \tag{49}$$

u is the tire longitudinal force:

$$u = \begin{bmatrix} F_{x1,l} & F_{x1,r} & F_{x2,l} & F_{x2,r} & F_{x3,l} & F_{x3,r} & F_{x4,l} & F_{x4,r} & F_{x5,l} & F_{x5,r} \end{bmatrix}^T \tag{50}$$

B is the coefficient matrix:

$$B = \left[\begin{array}{cccccccccc} \cos\delta_{1l} & \cos\delta_{1r} & \cos\delta_{2l} & \cos\delta_{2r} & \cos\delta_{3l} & \cos\delta_{3r} & \cos\delta_{4l} & \cos\delta_{4r} & \cos\delta_{5l} & \cos\delta_{5r} \\ \begin{pmatrix} -\frac{w}{2}\cos\delta_{1l} \\ +l_1\sin\delta_{1l} \end{pmatrix} & \begin{pmatrix} \frac{w}{2}\cos\delta_{1r} \\ +l_1\sin\delta_{1r} \end{pmatrix} & \begin{pmatrix} -\frac{w}{2}\cos\delta_{2l} \\ +l_2\sin\delta_{2l} \end{pmatrix} & \begin{pmatrix} \frac{w}{2}\cos\delta_{2r} \\ +l_2\sin\delta_{2r} \end{pmatrix} & \begin{pmatrix} -\frac{w}{2}\cos\delta_{3l} \\ -l_3\sin\delta_{3l} \end{pmatrix} & \begin{pmatrix} \frac{w}{2}\cos\delta_{3r} \\ -l_3\sin\delta_{3r} \end{pmatrix} & \begin{pmatrix} -\frac{w}{2}\cos\delta_{4l} \\ -l_4\sin\delta_{4l} \end{pmatrix} & \begin{pmatrix} \frac{w}{2}\cos\delta_{4r} \\ -l_4\sin\delta_{4r} \end{pmatrix} & \begin{pmatrix} -\frac{w}{2}\cos\delta_{5l} \\ -l_5\sin\delta_{5l} \end{pmatrix} & \begin{pmatrix} \frac{w}{2}\cos\delta_{5r} \\ -l_5\sin\delta_{5r} \end{pmatrix} \end{array} \right] \tag{51}$$

where τ is a 2-dimensional vector, u is a 10-dimensional vector, and B is a 2×10 matrix. The 10 vectors in u are the driving forces of each wheel of the distributed drive vehicle, which are mutually independent. This is clearly an underdetermined system with infinitely many solutions without other constraints.

Different tire longitudinal force distribution results will cause the in-wheel motors to output different driving torques, and the output efficiency of in-wheel motors will affect the vehicle's energy utilization efficiency and system stability margin. The tire longitudinal forces should maximize the vehicle and system's energy utilization efficiency and stability margin while satisfying the above constraints. This is a constrained optimization problem; therefore, corresponding objective functions can be established based on optimal control theory to achieve optimal distribution of wheel longitudinal forces for each axle.

The tire load rate is the ratio of the resultant force received by the tire from the ground to the maximum resultant force obtainable under these conditions, given the known tire vertical load and road adhesion coefficient. It is used to characterize the tire force margin and is an indicator of vehicle stability margin. Taking the left wheel as an example, its expression is as follows:

$$\rho_{xi,l} = \frac{\sqrt{\boldsymbol{F}_{xi,l}^2 + \boldsymbol{F}_{yi,l}^2}}{\mu \cdot \boldsymbol{F}_{zi,l}} \tag{52}$$

where $F_{zi,l}$ is the tire vertical force. The objective function of the controller is designed with the optimization objective of minimizing the sum of squares of tire load rates for all wheels:

$$J = \sum_{i=1}^{5} \left(\frac{\boldsymbol{F}_{xi,l}^2 + \boldsymbol{F}_{yi,l}^2}{(\mu \boldsymbol{F}_{zi,l})^2} + \frac{\boldsymbol{F}_{xi,r}^2 + \boldsymbol{F}_{yi,r}^2}{(\mu \boldsymbol{F}_{zi,r})^2} \right) \tag{53}$$

Since $F_{yi,l}$ and $F_{yi,r}$ are not control variables of the distribution layer and their values do not affect the optimal solution, Equation (53) can be written as

$$J = \sum_{i=1}^{5} \left(\frac{\boldsymbol{F}_{xi,l}^2}{(\mu \boldsymbol{F}_{zi,l})^2} + \frac{\boldsymbol{F}_{xi,r}^2}{(\mu \boldsymbol{F}_{zi,r})^2} \right) \tag{54}$$

The above optimization problem is formulated as follows:

$$\begin{cases} \min\limits_{\boldsymbol{F}_{xi(l,r)}} J = \sum\limits_{i=1}^{5} \left(\dfrac{\boldsymbol{F}_{xi,l}^2}{(\mu \boldsymbol{F}_{zi,l})^2} + \dfrac{\boldsymbol{F}_{xi,r}^2}{(\mu \boldsymbol{F}_{zi,r})^2} \right) \\ s.t. \quad \tau = B \cdot u \end{cases} \tag{55}$$

The torque that the in-wheel motor needs to provide can be obtained from the tire longitudinal force:

$$\begin{cases} \boldsymbol{T}_{xi,l} = \frac{\boldsymbol{F}_{xi,l} R_w}{i_g} \\ \boldsymbol{T}_{xi,r} = \frac{\boldsymbol{F}_{xi,r} R_w}{i_g} \end{cases} \tag{56}$$

where i_g is the in-wheel motor output efficiency. The finally obtained torque is input to the wheel torque input interface of the TruckSim model, directly acting on the wheels to simulate in-wheel motor driving and brake braking.

3.3. Neural Network-Based MPC Controller Design

The computational complexity of the MPC controller in the above control algorithm is relatively high, which affects system real-time performance to some extent, especially for the vehicle control unit (VCU) with limited computational power. The real-time performance of the control algorithm determines whether it can be applied to actual vehicles. To improve the real-time performance of the MPC controller, this paper adopts a neural network approximation method, achieving computational burden transfer through offline training and online inference strategies.

Considering the nonlinear characteristics of vehicle lateral dynamics and the computational constraints of actual vehicle platforms, a fully connected feedforward network is selected as the basic structure. The input layer contains four nodes: longitudinal vehicle speed v_x, sideslip angle at the center of gravity β, actual yaw rate ω_z, and desired yaw rate $\omega_{z,des}$. The hidden part adopts a three-layer design with node numbers of 64, 64, and 32, respectively. This structure was determined through systematic comparative experiments: among 15 network configurations containing different numbers of layers (2–4 layers) and nodes (16–128), the 64–64–32 structure achieved the optimal balance between control accuracy (MSE = 0.0053), inference efficiency (1.4 ms), and parameter scale (6568 parameters). The activation function adopts the ReLU function $f_x = \max(0, x)$, which has a concise form and high computational efficiency, while also helping to alleviate the gradient-vanishing problem in deep networks. The output layer includes five nodes, corresponding to the additional yaw moment ΔM_z and the active steering angles of axles 2 to 5: δ_2, δ_3, δ_4, δ_5.

Based on the TruckSim/Simulink co-simulation platform, tests were conducted within the vehicle speed range of 25 to 95 km/h at 5 km/h intervals. Each speed point underwent

15 s double-lane change maneuver simulation with a sampling frequency of 100 Hz, collecting a total of 22,500 valid samples. Data was normalized using Z-score standardization:

$$x_{norm} = \frac{x - \mu_x}{\sigma_x} \tag{57}$$

where μ_x and σ_x are the mean and standard deviation of corresponding variables in the training set, respectively. The training set and validation set were divided in a 9:1 ratio.

The loss function adopts a composite form, including the mean square loss of prediction errors and constraint violation penalties:

$$L = \frac{1}{N}\sum_{i=1}^{N}\|y_i - \hat{y}_i\|_2^2 + \lambda\sum_j \max(0, g_j(\hat{y}_i)) \tag{58}$$

where g_j represents the control constraint function.

The Adam algorithm was selected as the optimization algorithm, with an initial learning rate set to 0.005. The learning rate scheduling strategy adopts step decay, multiplying the learning rate by 0.1 every 20 epochs. The batch size was set to 1024, with a maximum training epoch limit of 80, combined with an early stopping mechanism to prevent overfitting. To evaluate generalization performance during training, 10% of the data was randomly reserved as a validation set. The loss function was evaluated on the validation set after each training epoch, and the model with minimum validation loss was saved as the final deployment model.

Although initial training enables the neural network to learn basic control strategies, control performance degradation or even instability may occur when facing edge conditions not fully covered by the training data. To address this, this paper employs a closed-loop incremental learning mechanism as shown in Figure 13, continuously improving the network's generalization capability through iterative optimization.

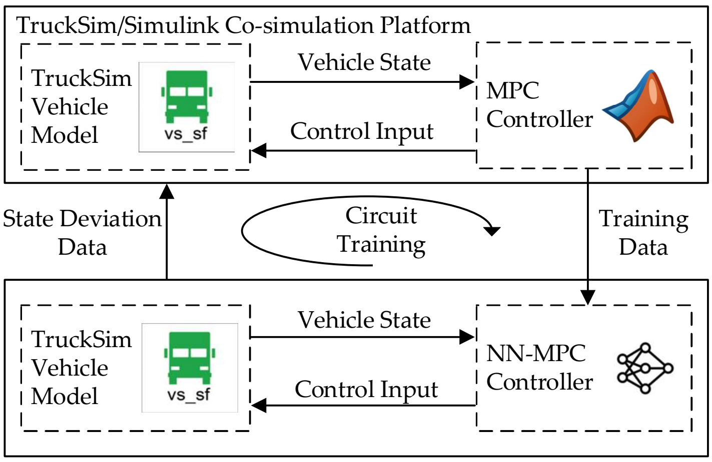

Figure 13. NN-MPC controller cyclic training process.

The incremental learning process is as follows: The initial neural network controller NN-MPC v1.0 is obtained through training with the base dataset. This controller replaces the original MPC controller and undergoes TruckSim/Simulink co-simulation experiments. By monitoring vehicle state variables, particularly changes in sideslip angle at the center of gravity and yaw rate, failure scenarios where control performance does not meet requirements are identified. For these failure scenarios, the original MPC controller is used for control to obtain optimal control outputs under corresponding states. These "teacher signals", together with corresponding state variables, form an augmented dataset. The augmented data is merged with the original training data to form a more comprehensive training sample set, and the neural network is retrained to obtain the improved version NN-MPC v2.0. This process iterates cyclically, with each iteration improving the neural network controller's generalization capability until no failure conditions occur under preset test conditions.

4. Experimental Verification

To fully validate the effectiveness of the proposed AWS/DYC coordinated control strategy in improving vehicle driving stability and expanding stability boundaries, targeted experimental schemes were designed based on the aforementioned experimental platform. Considering safety concerns for real vehicle tests, double-lane change simulation tests were conducted at 80 km/h vehicle speed with a road adhesion coefficient of 0.8 on the Simulink/TruckSim co-simulation platform to verify the control strategy's effectiveness under high-speed sharp-turning conditions. Real vehicle tests of double-lane change were conducted at 35 km/h on dry concrete road surfaces to preliminarily verify the deployment feasibility of the control strategy on actual vehicles.

4.1. High-Speed Condition Simulation Tests

High-speed simulation test results are shown in Figures 14–20. The comparison control strategies include no control and active rear-wheel steering control of axles 4 and 5 plus additional yaw moment control (ARS/DYC), where the ARS/DYC strategy is implemented based on the traditional MPC in Section 3.1; the AWS/DYC strategy is implemented based on the NN-MPC in Section 3.3. The prediction and control horizons for both the MPC controller in the ARS/DYC strategy and the MPC controller used for NN-MPC training in the AWS/DYC strategy are 15 steps, with a sampling period of 0.01 s and control frequency of 100 Hz.

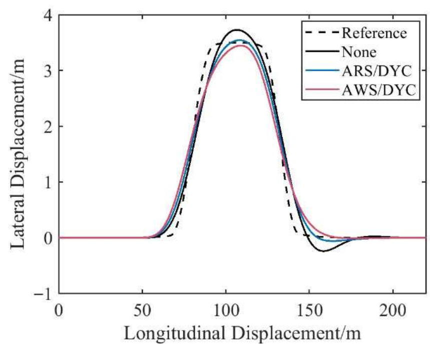

Figure 14. Driving trajectory comparison (High-Speed Simulation Tests).

(1) Yaw Dynamics Characteristics Analysis

From the yaw rate response characteristics shown in Figure 15, the AWS/DYC coordinated control strategy demonstrates significant superiority. During the final steering return phase, this strategy limits the yaw rate peak to within 0.122 rad/s, achieving peak suppression effects of 41.04% and 21.62% compared to the uncontrolled baseline condition and ARS/DYC control scheme, respectively. Considering that the desired yaw rate $\omega_{z,des}$ for each control algorithm is determined by the steady-state gain $G_{\omega_z ss}$ of front-axle steering input to ω_z and road adhesion coefficient μ, these results fully demonstrate that the AWS/DYC strategy can significantly reduce the driver's steering control burden while improving vehicle steering response characteristics and path-tracking accuracy.

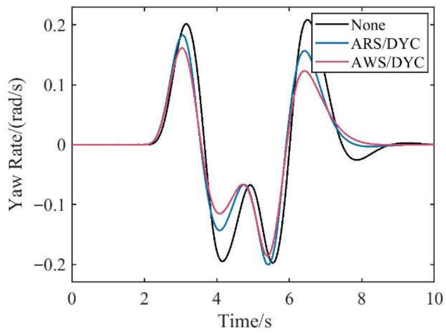

Figure 15. Yaw rate comparison (High-Speed Simulation Tests).

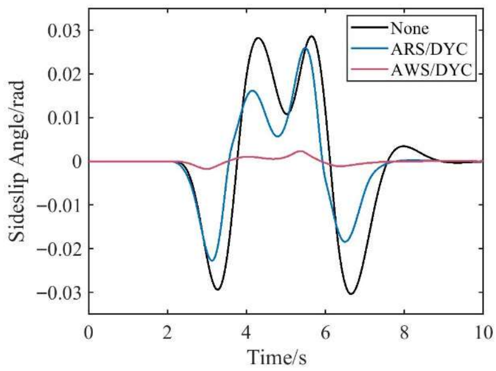

Figure 16. Sideslip angle comparison (High-Speed Simulation Tests).

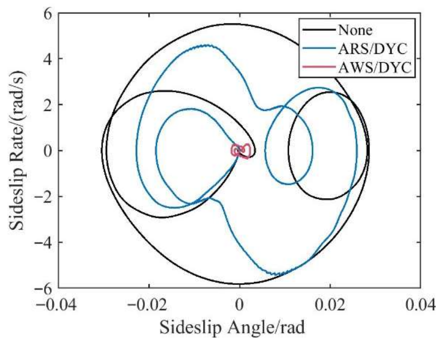

Figure 17. Phase plane comparison (High-Speed Simulation Tests).

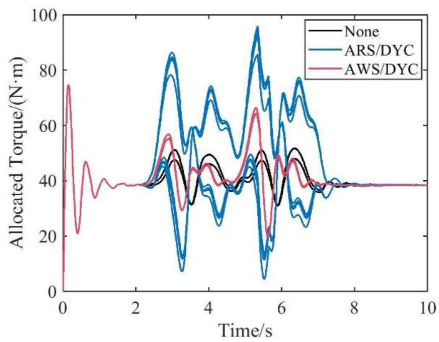

Figure 18. Distributed torque comparison (High-Speed Simulation Tests).

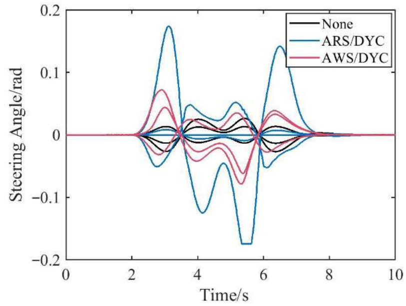

Figure 19. Active steering angle comparison (High-Speed Simulation Test).

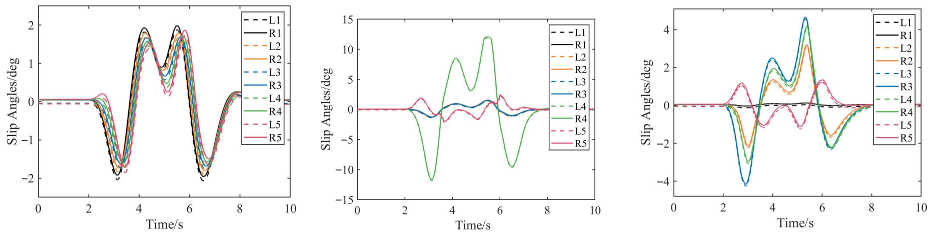

(**a**) (**b**) (**c**)

Figure 20. Comparison of tire slip angles under different control strategies: (**a**) uncontrolled; (**b**) ARS/DYC control; (**c**) AWS/DYC control.

(2) Lateral Stability Assessment

The sideslip angle at the center of gravity, as a key indicator for evaluating vehicle lateral stability, shows a dynamic response as seen in Figure 16. The AWS/DYC coordinated control exhibits excellent sideslip angle suppression capability, controlling its peak amplitude within an extremely small range of 0.0023 rad, with peak suppression rates of 92.31% and 90.98% compared to the baseline state and ARS/DYC scheme, respectively. This control strategy ensures the sideslip angle consistently maintains near zero, fundamentally enhancing the vehicle's lateral stability margin. Combined with the trajectory tracking results analysis shown in Figure 14, during the continuous steering process of double-lane change conditions, both uncontrolled and ARS/DYC controlled vehicles exhibit obvious fishtailing and sideslip instability characteristics, while AWS/DYC coordinated control maintains good attitude control capability. The $\beta - \dot{\beta}$ phase plane trajectory shown in Figure 17 further validates this conclusion, with the phase trajectory under AWS/DYC control presenting high convergence characteristics, its envelope area reduced by 99.69% and 99.45% relative to the baseline condition and ARS/DYC scheme, respectively, indicating the system has an extremely strong stability margin.

(3) Actuator Saturation Characteristics Analysis

Figure 18 reveals the driving torque distribution characteristics under different control strategies. AWS/DYC coordinated control limits the maximum single-wheel driving torque demand to 66.12 N · m, 30.78% lower than the ARS/DYC strategy, and below the in-wheel motor's rated output capability of 70.0 N·m. This result indicates that the AWS/DYC strategy effectively avoids actuator saturation problems while ensuring control performance, improving the system's engineering feasibility on distributed drive heavy-duty vehicle platforms.

(4) Steering Angle Distribution Strategy Comparison

The steering angle distribution results shown in Figure 19 indicate that AWS/DYC coordinated control adopts an all-wheel coordinated steering mode, with a maximum steering angle amplitude of 0.079 rad (4.53°), increased by 193.48% relative to traditional Ackermann steering geometry but still maintained within reasonable range. In contrast, the ARS/DYC strategy concentrates control action on the rear-wheel steering of axles 4 and 5, with the steering angle peak reaching the preset 10° constraint boundary (551.07% increase from Ackermann baseline), yet the stability improvement effect does not show a corresponding proportional relationship. Excessive steering angles not only aggravate tire wear but may also trigger tire lateral force saturation. Therefore, the all-wheel coordinated steering mode of AWS/DYC fully exploits the control potential of multi-axle independent steering systems through reasonable angle distribution, achieving optimal balance between control performance and engineering constraints. Figure 20 presents the comparison of tire slip angles under three control strategies. Without control, the slip angles across all wheels are uniformly distributed and low (~1.9° maximum), significantly below the linear working region (~5°), indicating that tire lateral performance is underutilized. The ARS/DYC control substantially increases slip angles, with the rear axle reaching 11.9°, exceeding the linear region and entering saturation, where lateral force growth plateaus, risking stability loss. AWS/DYC control maintains relatively uniform slip angle distribution across axles with a maximum of 4.7°, entirely within the linear region, optimally balancing performance utilization with lateral stability while preserving a safety margin.

(5) Real-time Performance Analysis

The simulation time comparison in Table 3 reveals significant performance improvements. Under the same simulation environment (Intel Ultra 7 CPU, 32 GB RAM), the time consumption for 10 s double-lane change condition simulation is compared as follows: baseline time without control is 6.97 s, mainly due to TruckSim vehicle model computation; MPC-based ARS/DYC control strategy takes 19.38 s, with the additional 12.41 s mainly used for MPC online optimization solving; AWS/DYC control strategy using NN-MPC takes 8.42 s, only 1.45 s more than the uncontrolled case. Compared to ARS/DYC(MPC), simulation time is reduced by 56.55%, and after deducting the basic time consumption of the TruckSim model, the pure control algorithm computational efficiency improves by 88.32%. Notably, AWS/DYC's MPC control variables (one additional yaw moment plus four active steering angles) are two more than ARS/DYC (one additional yaw moment plus two active steering angles), with higher optimization problem complexity, but NN-MPC still achieves significant speed improvement, fully demonstrating the advantages of the neural network approach. This substantial improvement in computational efficiency has important significance for actual deployment, especially under limited computational resources of vehicle control units, where NN-MPC can reserve sufficient computational resources for other functional modules (such as perception and planning) while ensuring control performance.

Table 3. Simulation time comparison.

No.	Control Strategy	Running Time (s)
1	None	6.97
2	ARS/DYC (MPC)	19.38
3	AWS/DYC (NN-MPC)	8.42

4.2. Low-Speed Real Vehicle Tests

Low-speed real vehicle tests were conducted at a closed test site, with a selected vehicle speed of 35 km/h on a dry concrete road surface (adhesion coefficient $\mu \approx 0.8$), providing repeatable test conditions approaching vehicle lateral dynamics limits. The test condition selected the representative double-lane change handling stability test condition, with the real vehicle test scenario shown in Figure 21.

Figure 21. Real vehicle test scenario.

Real vehicle test double-lane change condition comparison results are shown in Figures 22–27:

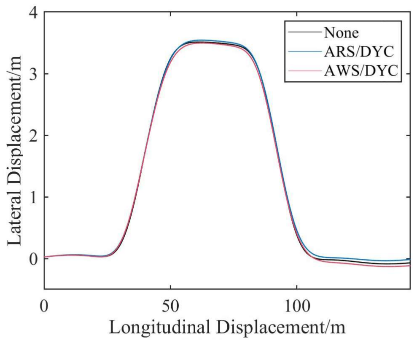

Figure 22. Driving trajectory comparison (Low-Speed Real Vehicle Tests).

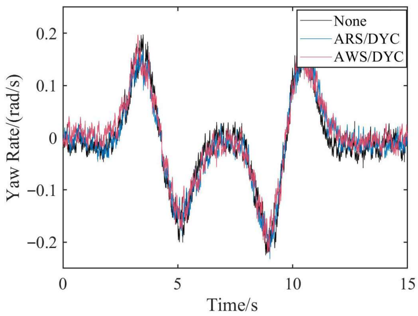

Figure 23. Yaw rate comparison (Low-Speed Real Vehicle Tests).

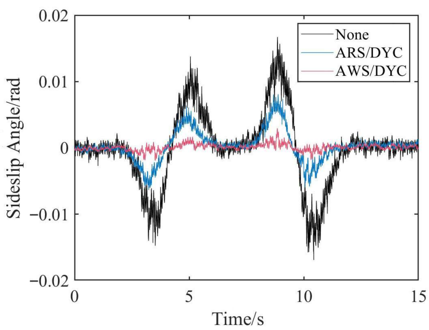

Figure 24. Sideslip angle comparison (Low-Speed Real Vehicle Tests).

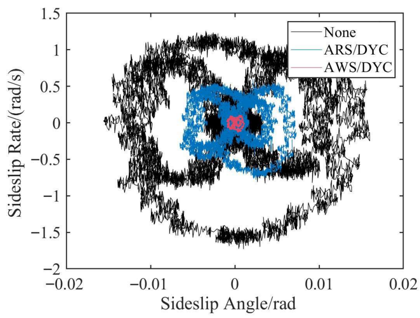

Figure 25. Phase plane comparison (Low-Speed Real Vehicle Tests).

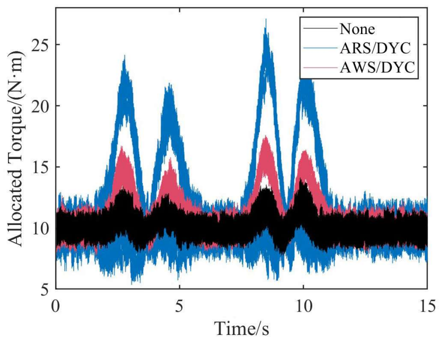

Figure 26. Distributed torque comparison (Low-Speed Real Vehicle Tests).

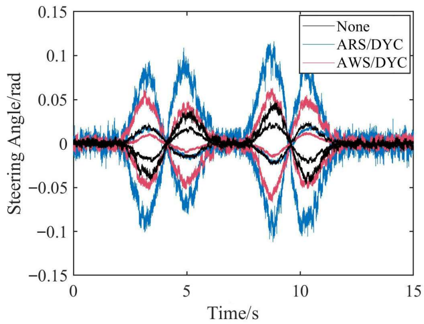

Figure 27. Active steering angle comparison (Low-Speed Real Vehicle Tests).

Figure 22 presents the trajectory comparison under no control, ARS/DYC control, and AWS/DYC control strategies. Results indicate that vehicles under all three control modes can accurately track the predetermined trajectory, with trajectory deviations within an acceptable range.

(1) Yaw Dynamics Characteristics Analysis

Figure 23 provides the yaw rate comparison results. At the test speed of 35 km/h, yaw rate peaks under AWS/DYC and ARS/DYC control strategies are slightly lower than the uncontrolled state, but the differences are not significant. This phenomenon can be explained from two aspects: on one hand, lower vehicle speed makes lateral dynamics response relatively mild, with control effect differences less obvious than high-speed conditions; on the other hand, under the same trajectory tracking and steering wheel angle input conditions, yaw response differences at low-speed conditions are inherently smaller.

(2) Stability Control Effect Analysis

Sideslip angle at the center of gravity is a key indicator for evaluating vehicle stability. As shown in Figure 24, the AWS/DYC control strategy significantly improves vehicle stability: under AWS/DYC control strategy, sideslip angle consistently maintains small fluctuations near zero; compared to the uncontrolled state, the sideslip angle peak is reduced by 0.00901 rad, a decrease of 96.47%; compared to the ARS/DYC control strategy, the sideslip angle peak is reduced by 0.00322 rad, a decrease of 66.19%, effectively suppressing potential "understeer" and "oversteer" tendencies (although these phenomena are not obvious at low-speed conditions). The $\beta - \dot{\beta}$ phase plane diagram shown in Figure 25 further validates the above conclusions. The phase trajectory envelope area under the AWS/DYC control strategy is significantly reduced, almost converging near the origin at low-speed conditions, fully demonstrating the control strategy's enhancement effect on vehicle stability.

(3) Actuator Output Characteristics Analysis

Figure 26 shows the torque distribution of each in-wheel motor under three control strategies. Comparative analysis shows the following: under the uncontrolled state, each in-wheel motor torque is basically the same and remains constant, only used to maintain vehicle speed; under the ARS/DYC control strategy, torque peak increases by 12.38 $\mathrm{N \cdot m}$ compared to the uncontrolled state; AWS/DYC reduces torque peak by 8.64 $\mathrm{N \cdot m}$ compared to the ARS/DYC control strategy, a decrease of 33.59%. The dynamic torque distribution reflects the proactiveness of control strategies, achieving the tracking of ideal yaw rate and suppression of sideslip angle through differential torque.

(4) Active Steering Control Analysis

Figure 27 compares the steering angle changes of each axle wheel. Results show the following: under the uncontrolled state, each axle steering angle follows the traditional Ackermann steering geometry relationship; under the ARS/DYC control strategy, the active steering angle peak increases by 0.065 rad compared to the uncontrolled state; AWS/DYC reduces the active steering angle peak by 0.048 rad compared to the ARS/DYC control strategy, a decrease of 44.91%.

The larger camber angle change of inner wheels shown in Figure 21 results from suspension geometry changes caused by vehicle body roll during turning, which is a suspension kinematics characteristic. Not considering this factor in modeling is mainly based on two points: first, the tire camber angle change amplitude of actual multi-axle special vehicles is much smaller than the test prototype vehicle; second, the vehicle dynamics model established in this paper focuses on longitudinal, lateral, and yaw three-degrees-of-freedom dynamics characteristics, which sufficiently characterize the main features of vehicle-handling stability. The impact of this suspension kinematics phenomenon on lateral stability control strategy validation can be neglected.

Comprehensive high-speed simulation and low-speed real vehicle test results indicate that the proposed AWS/DYC coordinated control strategy exhibits significant advantages: high-speed simulation tests verified the strategy's excellent stability control performance under extreme conditions, improving the vehicle stability margin to near-ideal levels in high-adhesion road emergency obstacle avoidance conditions, effectively suppressing sideslip instability risks; low-speed real vehicle tests preliminarily verified the control algorithm's engineering deployability and real-time performance. Compared to the ARS/DYC strategy constrained by traditional Ackermann steering geometry, AWS/DYC achieves better stability control effects while reducing actuator demands through all-wheel coordinated dynamic optimal distribution, fully demonstrating the architecture's theoretical advantages and engineering application potential. It should be noted that limited by safety factors, current real vehicle tests were only conducted under low-speed stable conditions, unable to fully verify the control strategy's extreme performance. Subsequent research will gradually increase test speeds and expand to more complex road conditions to comprehensively evaluate the control system's robustness.

5. Conclusions

This paper conducts research on vehicle control algorithms for a distributed drive five-axle test platform, aiming to maintain vehicle-handling stability while reducing in-wheel motor output torque. First, a TruckSim vehicle model was established based on vehicle parameters, and its accuracy was verified through real vehicle tests. Then, a three-degrees-of-freedom dynamic model including vehicle longitudinal, lateral, and yaw dynamics was established. Considering the operating characteristics of multi-axle vehicles, an LPV tire model was used to improve the calculation accuracy of tire lateral forces. For stability control, based on direct yaw moment control, all-wheel steering control, and an MPC algorithm, a hierarchical stability control architecture for multi-axle vehicles was proposed, integrating multi-variable coordinated control with decoupled drive, brake, and steering control. The upper-layer MPC controller determines the additional yaw moment and wheel active steering angles required to maintain an ideal yaw rate and sideslip angle at the center of gravity, while a fuzzy controller dynamically adjusts MPC control weights, and a PID controller calculates the longitudinal force required for tracking target vehicle speed. The lower-layer controller allocates control variables with the objective of minimizing tire load rate. To facilitate deployment on a vehicle control unit (VCU), a neural network approach was introduced, training neural network controllers using input–output data from model predictive controllers to improve the real-time performance of control algorithms. Finally, high-speed simulation tests and low-speed real vehicle tests were conducted, respectively. Results show that compared to the no-control strategy and active rear-wheel steering plus direct yaw moment control strategy, the proposed control strategy significantly improves vehicle-handling stability while reducing in-wheel motor output torque, with more flexible active steering strategy and better controller real-time performance. This research fully leverages the advantages of the distributed drive configuration and has important significance for its application in multi-axle vehicles and improving multi-axle vehicle safety.

However, the current research also has certain limitations. First, the current LPV tire model parameters are based on offline identification, without considering the effects of tire wear, temperature variations, and other factors on the model parameters. Second, although the neural network controller adopts incremental learning, it mainly relies on simulation data with limited adaptability to parameter perturbations and unmodeled dynamics in actual operation, facing challenges of high training costs and insufficient generalization capability. Finally, while distributed drive systems have inherent redundancy, this paper has not deeply studied fault-tolerant control strategies under single or multiple in-wheel motor and steering actuator failures, which is crucial for improving system reliability. Future research should focus on the following aspects: first, exploring the construction of adaptive control strategies, consider introducing online parameter identification methods based on recursive least squares or Kalman filtering to achieve real-time updating of LPV tire model parameters; second, attempting to introduce methods such as reinforcement learning, enabling controllers to continuously optimize strategies through continuous interaction with the environment, enhancing adaptability to unexpected conditions; and finally, attempting to construct an active fault-tolerant control framework, establishing diagnosis and localization mechanisms for actuator failures and studying how to achieve effective fault-tolerant control through control allocation reconfiguration, thereby ensuring that basic vehicle stability can be maintained even when partial actuators fail.

Author Contributions: Conceptualization, Z.H.; methodology, H.C.; software, Z.H.; validation, J.L. and J.Z.; writing—original draft preparation, Y.Z.; writing—review and editing, X.L.; project

administration, Z.L.; funding acquisition, Z.L. All authors have read and agreed to the published version of the manuscript.

Funding: This research was funded by the National Natural Science Foundation of China "Load-bearing and Stability Enhancement Control Technology for Multi-axle Distributed Drive Special Vehicles", grant number 52472464; Young Star of Science and Technology in Shaanxi Province (Grant No. 2025ZC-KJXX-84) and Sanqin Talent Special Support Program of Shaanxi Province.

Data Availability Statement: Data are contained within the article.

Acknowledgments: The authors thank Bojun Zhou for his great support in the writing of this paper.

Conflicts of Interest: The authors declare no conflicts of interest. Informed consent for participation was obtained from all subjects involved in the study.

References

1. Zhang, X.; Cheng, Q.; Du, H.; Wan, J. A novel energy-saving steering control strategy based on general power model for multiaxle steer-by-wire vehicles. *IEEE Trans. Ind. Electron.* **2025**, *72*, 8440–8450. [CrossRef]
2. Liu, J.; Zhang, C.; Shi, C.; Lin, B.; Wu, D. Steering control for handling and stability and wear resistance of multi-axle vehicles. *Veh. Syst. Dyn.* **2025**, *63*, 825–852. [CrossRef]
3. Yang, M.; Xu, C.; Yan, M. Decentralized compliance control for multi-axle heavy vehicles equipped with electro-hydraulic actuator suspension systems. *Sensors* **2025**, *25*, 5456. [CrossRef] [PubMed]
4. Li, Z.; Pan, S.; Mao, K.; Xu, Y. Combined acceleration slip regulation for multi-wheel distributed electric drive vehicles considering torque loss factor. *Control Eng. Pract.* **2024**, *146*, 105893. [CrossRef]
5. Li, Y.; Cai, Y.; Sun, X.; Wang, H.; Chen, L.; Lian, Y.; Dong, Z. Distributed modeling and scenario-driven extension hybrid-dmpc coordinated control of autonomous vehicle chassis. *IEEE Trans. Intell. Transp. Syst.* **2025**, *26*, 7186–7196. [CrossRef]
6. Deng, H.; Zhao, Y.; Nguyen, A.-T.; Huang, C. Fault-tolerant predictive control with deep-reinforcement-learning-based torque distribution for four in-wheel motor drive electric vehicles. *IEEE-ASME Trans. Mechatronics* **2023**, *28*, 668–680. [CrossRef]
7. Jin, Z.; Wang, C.; Zhang, L.; Zhao, W.; Khajepour, A. Rollover prevention for a heavy vehicle using optimised slide mode steering control. *Int. J. Heavy Veh. Syst.* **2019**, *26*, 351–374. [CrossRef]
8. Yue, M.; Shangguan, J.; Guo, L.; Zhao, J. All-in-one control framework for distributed drive electric buses path tracking subject to uncertain crosswind and varied passenger mass. *IEEE Trans. Veh. Technol.* **2023**, *72*, 8342–8353. [CrossRef]
9. Liang, J.; Lu, Y.; Yin, G.; Fang, Z.; Zhuang, W.; Ren, Y.; Xu, L.; Li, Y. A distributed integrated control architecture of afs and dyc based on mas for distributed drive electric vehicles. *IEEE Trans. Veh. Technol.* **2021**, *70*, 5565–5577. [CrossRef]
10. Zhang, H.; Wang, J. Active steering actuator fault detection for an automatically-steered electric ground vehicle. *IEEE Trans. Veh. Technol.* **2017**, *66*, 3685–3702.
11. Li, S.; Wang, X.; Cui, G.; Lu, X.; Zhang, B. Yaw and lateral stability control based on predicted trend of stable state of the vehicle. *Veh. Syst. Dyn.* **2023**, *61*, 111–127. [CrossRef]
12. Qiang, Z.; Dai, L.; Chen, B.; Xia, Y. Model predictive control for on-ramp vehicle merging to a platoon on main road in finite time. *IEEE Trans. Intell. Transp. Syst.* **2025**, *26*, 4731–4743. [CrossRef]
13. Zhou, X.; Liu, R.; Zhou, J.; Zhang, Z.; Wang, C.; Zhao, W. Robust tube-mpc trajectory tracking control for four-wheel independent steering vehicles on intermittent snowy and icy roads. *Chin. J. Mech. Eng.* **2025**, *38*, 65. [CrossRef]
14. Chen, W.; Wang, J.; Zhang, T.; Li, G.; Jin, Y.; Ge, L.; Zhou, M.; Tan, C.-W. Exploring symmetry-induced divergence in decentralized electric vehicle scheduling. *IEEE Trans. Ind. Appl.* **2024**, *60*, 1117–1128. [CrossRef]
15. Xie, Y.; Lu, G.; Zheng, F.; Cao, P.; Liu, X. A hierarchical approach for integrating merging sequencing and trajectory optimization for connected and automated vehicles. *IEEE Trans. Intell. Transp. Syst.* **2024**, *25*, 7552–7567. [CrossRef]
16. Zhang, Z.; Wang, W.; Liang, J.; Zhao, W.; Pan, C. Mixed platoon hierarchical control: Elevating safety, stability, and efficiency in cav-hv integration. *IEEE Trans. Intell. Transp. Syst.* **2025**, *26*, 8397–8410. [CrossRef]
17. Li, Z.; Wang, P.; Cai, S.; Hu, X.; Chen, H. NMPC-based controller for vehicle longitudinal and lateral stability enhancement under extreme driving conditions. *ISA Trans.* **2023**, *135*, 509–523. [CrossRef] [PubMed]
18. Li, H.; Hu, Z.; Li, J.; Hu, J.; Xu, L.; Ouyang, M. A comprehensive analysis on electronic moment power steering control strategy for multi-axle distributed drive vehicles. *Automot. Innov.* **2024**, *7*, 507–528. [CrossRef]
19. Shi, X.; Wang, H.; Cai, Y.; Sun, X.; Chen, L.; Yang, C. Two-stage auxiliary drifting path tracking control for distributed driving three-axle commercial vehicles. *ISA Trans.* **2024**, *153*, 404–419. [CrossRef]
20. Ataei, M.; Khajepour, A.; Jeon, S. Model predictive control for integrated lateral stability, traction/braking control, and rollover prevention of electric vehicles. *Veh. Syst. Dyn.* **2020**, *58*, 49–73. [CrossRef]

21. Beal, C.E.; Gerdes, J.C. Model predictive control for vehicle stabilization at the limits of handling. *IEEE Trans. Control Syst. Technol.* **2013**, *21*, 1258–1269. [CrossRef]
22. Li, Z.; Li, J.; Min, Q.; Liu, B. A fast-computing path tracking control strategy for autonomous multiaxle electric vehicle considering safety and stability. *IEEE Trans. Transp. Electrif.* **2024**, *10*, 6024–6038. [CrossRef]
23. Li, Z.; Li, J.; Li, Y. An integrated path planning framework for multi-obstacle avoidance of the multi-axle autonomous vehicle with enhanced safety and stability. *IEEE Trans. Veh. Technol.* **2024**, *73*, 6368–6382. [CrossRef]
24. Li, Z.; Li, J.; Wang, W. Path planning and obstacle avoidance control for autonomous multi-axis distributed vehicle based on dynamic constraints. *IEEE Trans. Veh. Technol.* **2023**, *72*, 4342–4356. [CrossRef]
25. Khodaverdian, A.; Gohil, D.; Christofides, P.D. Neural network implementation of model predictive control with stability guarantees. *Digit. Chem. Eng.* **2025**, *16*, 100262. [CrossRef]
26. Hassan, A.; Ruiz-Moreno, S.; Frejo, J.R.D.; Maestre, J.M.; Camacho, E.F. Neural-network based mpc for enhanced lateral stability in electric vehicles. *IEEE Access* **2024**, *12*, 23265–23278. [CrossRef]
27. Liu, X.; Wang, W.; Li, X.; Liu, F.; He, Z.; Yao, Y.; Ruan, H.; Zhang, T. MPC-based high-speed trajectory tracking for 4wis robot. *ISA Trans.* **2022**, *123*, 413–424. [CrossRef]
28. Wu, Y.; Li, B.; Zhang, N.; Du, H.; Zhang, B. Rear-steering based decentralized control of four-wheel steering vehicle. *IEEE Trans. Veh. Technol.* **2020**, *69*, 10899–10913. [CrossRef]
29. Chu, Y.; Wang, C.; Zhou, X.; Zhang, Z.; Zhao, W. Instantaneous center of rotation tracking control of four-wheel independent steering vehicles under large-curvature turning conditions. *IEEE Trans. Intell. Transp. Syst.* **2024**, *25*, 17965–17978. [CrossRef]
30. Jneid, M.S.; Harth, P. Integrated torque vectoring control using vehicle yaw rate and sideslip angle for improving steering and stability of all offwheel-motor drive electric vehicles. *Acta Polytech. Hung.* **2024**, *21*, 87–106. [CrossRef]
31. Amato, G.; Marino, R. Reconfigurable slip vectoring control in four in-wheel drive electric vehicles. *Actuators* **2021**, *10*, 157. [CrossRef]
32. Dahmani, H.; Pagès, O.; Hajjaji, A.E.; Daraoui, N. Observer-based robust control of vehicle dynamics for rollover mitigation in critical situations. *IEEE Trans. Intell. Transp. Syst.* **2014**, *15*, 274–284. [CrossRef]
33. Shi, Q.; Zhang, H. An improved control-oriented tire model and its applications on intelligent vehicles. *IEEE Trans. Intell. Veh.* **2024**, *9*, 1501–1511. [CrossRef]